

DIAMAGNETIC FLUX MEASUREMENTS ON THE
STOR-M TOKAMAK

A Thesis Submitted to the
College of Graduate Studies and Research
in Partial Fulfillment of the Requirements
for the degree of Master of Science
in the Plasma Physics Laboratory of Physics and Engineering
Physics
University of Saskatchewan
Saskatoon

By

Dallas John Trembach

©Dallas John Trembach, April 2009. All rights reserved.

PERMISSION TO USE

In presenting this thesis in partial fulfilment of the requirements for a Postgraduate degree from the University of Saskatchewan, I agree that the Libraries of this University may make it freely available for inspection. I further agree that permission for copying of this thesis in any manner, in whole or in part, for scholarly purposes may be granted by the professor or professors who supervised my thesis work or, in their absence, by the Head of the Department or the Dean of the College in which my thesis work was done. It is understood that any copying or publication or use of this thesis or parts thereof for financial gain shall not be allowed without my written permission. It is also understood that due recognition shall be given to me and to the University of Saskatchewan in any scholarly use which may be made of any material in my thesis.

Requests for permission to copy or to make other use of material in this thesis in whole or part should be addressed to:

Head of the Department of Physics and Engineering Physics

116 Science Place

University of Saskatchewan

Saskatoon, Saskatchewan

Canada

S7N 5E2

ABSTRACT

Diamagnetic measurements of poloidal beta have been performed in the STOR-M tokamak by a flux loop placed exterior to the vacuum chamber. Poloidal beta is defined as the ratio of plasma kinetic pressure to poloidal magnetic field pressure. Compensation for the vacuum toroidal field has been performed using a non-enclosing co-planar coil, and vibrational compensation from auxiliary coils. It was found that in STOR-M conditions (20% toroidal magnetic field decay over discharge) there is significant influence on the diamagnetic flux measurements from strong residual signals, presumably from image currents being induced by the toroidal field coils, requiring further compensation. A blank (non-plasma) shot is used specifically to eliminate the residual component which is not proportional to the toroidal magnetic field. Data from normal ohmic discharge operation is presented and calculations of poloidal beta from coil data ($\beta_\theta \simeq 0.5$) is found to be in reasonable agreement with the values of poloidal beta obtained from measurements of electron density and Spitzer temperature with neoclassical corrections for trapped electrons. Contributions present in the blank shot (residual) signal and the limitations of this method are discussed. A pulse with Compact Toroid Injection was examined and compared to a normal ohmic discharge, and one where the Compact Toroid Injector was used to supply the tokamak with neutral gas. Soft X-Ray (SXR) measurements were taken and compared. There is a strong agreement between the profiles of the poloidal beta and the SXR measurements. The bulk plasma thermal energy was measured and found to increase by 5.6 J following the injection of a CT. The diamagnetic measurements appear to be affected by image currents induced in the chamber walls by the plasma current, and also by plasma position fluctuations. Future work outlining the possibility of compensating these currents and improving the measurements is presented.

ACKNOWLEDGEMENTS

I would like to thank Dr. Akira Hirose for serving as supervisor and chief motivator during this project. Dr. Hirose's guidance has been instrumental in developing research and scientific skills throughout this project. His demand for excellence has fostered in me a drive and motivation that I hope will bring great success in the future. It has truly been a priveledge to work with Dr. Hirose.

Dr. Chijin Xiao is owed a debt of gratitude for his constant tutelage and guidance. I have very much enjoyed a continued master and apprentice relationship with him, and feel I have gained tremendously from his wisdom and experience.

Dr. Micheal Bradley has been both friend and professor throughout my education. I am grateful for our many discussions. I would also like to thank Dr. Tse for giving me the chance to truly experience research during my 4th year of undergraduate education. Thanks go to Dave McColl for his discussions, instruction, technical experience, and general comradery. I would also like to thank Dr. Mykola Dreval who has been an excellent colleague. As well, my fellow graduate students, the machine shop crew, and many people around campus have all contribute to my experience here.

This work is dedicated to my family

CONTENTS

| | |
|--|-------------|
| Permission to Use | i |
| Abstract | ii |
| Acknowledgements | iii |
| Contents | v |
| List of Tables | vii |
| List of Figures | viii |
| List of Abbreviations | x |
| List of Symbols | xi |
| 1 Introduction | 1 |
| 1.1 Motivation | 1 |
| 1.2 Principles of Magnetic Fusion | 1 |
| 1.2.1 A Brief History of Fusion | 1 |
| 1.2.2 Deuterium-Tritium Reaction | 3 |
| 1.2.3 Plasmas | 4 |
| 1.2.4 Plasmas in Magnetic Fields | 6 |
| 1.3 Diamagnetism and Paramagnetism of Plasmas in Tokamaks | 8 |
| 1.4 Thesis Outline | 14 |
| 2 Magnetohydrodynamic Equilibrium | 16 |
| 2.1 Equilibrium in the Minor Radial Direction | 16 |
| 2.2 Bulk Plasma Thermal Energy and the Energy Confinement Time | 20 |
| 3 Machine Description | 22 |
| 3.1 STOR-M Tokamak | 22 |
| 3.2 Vacuum Chamber and Gas Feed Systems | 23 |
| 3.3 Magnetic Field Systems | 24 |
| 3.3.1 Toroidal Field System | 26 |
| 3.3.2 Poloidal Field System | 26 |
| 3.3.3 Position Feedback Control System | 27 |
| 3.4 Compact Toroid Injection System | 29 |
| 3.5 Soft X-Ray | 29 |
| 3.6 Interferometer | 30 |
| 3.7 Rogowski Coils and Voltage Loop | 31 |
| 3.8 Spitzer Temperature | 32 |

| | | |
|----------|---|-----------|
| 4 | Experimental Configuration | 35 |
| 4.1 | Methods of Diamagnetic Measurements | 35 |
| 4.1.1 | Measurement of Toroidal Feed Lines | 35 |
| 4.1.2 | Method of Compensated loops | 36 |
| 4.1.3 | Method employed on STOR-1M | 37 |
| 4.2 | Implementation of Coils on STOR-M | 37 |
| 4.2.1 | Requirements for STOR-M | 37 |
| 4.2.2 | Primary Compensation | 38 |
| 4.2.3 | Vibrational Compensation | 39 |
| 4.2.4 | Effect of Chamber Walls | 40 |
| 4.2.5 | Baseline Compensation Methodology | 43 |
| 4.2.6 | Coil Design | 47 |
| 4.2.7 | Coil properties | 49 |
| 4.3 | Error Budget | 49 |
| 5 | Experimental Results | 52 |
| 5.1 | Experimental Outline | 52 |
| 5.2 | Ohmic Discharge Experiments | 52 |
| 5.3 | Compact Toroid Injection Experiments | 56 |
| 5.4 | Summary of Experimental Results | 59 |
| 5.4.1 | Ohmic Discharge Experiments | 59 |
| 5.4.2 | Compact Toroid Injection Experiments | 59 |
| 6 | Conclusion and Future Work | 63 |
| 6.1 | Conclusion | 63 |
| 6.2 | Future Work | 64 |
| 6.2.1 | Compensation of Chamber Image Currents | 64 |
| 6.2.2 | Internal Measurements | 66 |
| 6.2.3 | Improved Signal Processing | 66 |
| 6.2.4 | Diamagnetic Measurements in the Proposed STOR-U Tokamak | 69 |
| | References | 78 |
| A | Installation notes for the Diamagnetic Coil | 79 |
| A.1 | Diamagnetic Coil | 79 |
| A.1.1 | Parameters | 79 |
| A.1.2 | Coil Winding Notes | 79 |
| A.1.3 | Installation Figures | 83 |
| A.1.4 | Installation Notes | 85 |
| A.1.5 | Removal Notes | 85 |
| A.2 | Signal Processing | 86 |
| A.2.1 | BNC Breakout Box | 86 |
| A.2.2 | DA 15 Pinout Diagram | 87 |

LIST OF TABLES

| | | |
|-----|--|----|
| 3.1 | STOR-M Parameters | 23 |
| 3.2 | USCTI Parameters | 30 |
| 4.1 | Inductance, Capacitance, and Resistance measurements of the Diamagnetic Coils. Properties are shown for the single loop coil (Dm), the primary compensation coil (P), the inner auxiliary coil (Ai) and the outer auxiliary coil (Ao). | 50 |
| 4.2 | Eliminated Errors for Diamagnetic Diagnostics | 50 |
| 4.3 | Remaining Error Budget for Diamagnetic Diagnostics | 51 |
| A.1 | DA 15 Pinout (26 July 2007) | 87 |

LIST OF FIGURES

| | | |
|-----|---|----|
| 1.1 | Advances in Fusion Research. | 2 |
| 1.2 | Conceptual illustration of matter becoming a plasma. Water begins as a solid (ice) and with heat becomes a liquid, then with further heating becomes a gas. With continued heating, the atoms making up the water molecule disassociate and ionize, becoming plasma. | 4 |
| 1.3 | Simplified schematic diagram showing the major magnetic components of a tokamak, and the resultant magnetic field. Toroidal field coils, Ohmic heating coils (inner set) and vertical field coils (outer set) can are shown. | 7 |
| 1.4 | Current density components are shown for (a) plasma current flowing with the toroidal magnetic field, and (b) plasma current flowing opposite to the toroidal magnetic field. In both cases, the flux due to J_θ adds to the applied field (paramagnetism). | 9 |
| 1.5 | Model of plasma diamagnetism showing net current drift J_\perp , plasma pressure gradient ∇p , and expansion force $\mathbf{F}_{\nabla p}$ | 11 |
| 1.6 | A charged particle gyrating about a magnetic field line. | 12 |
| 2.1 | The plasma torus is approximated as a cylindrical plasma. The toroidal component is treated as the z axis. | 17 |
| 3.1 | Overhead sketch of the STOR-M Tokamak showing diagnostics. Insert shows limiter cross section. | 22 |
| 3.2 | Vertical cross section scale diagram of the STOR-M Tokamak showing magnetic coils. OH refers to the ohmic heating coils used for heating. VE refers the the vertical field coils used to obtain equilibrium. FB refers to the feed back coils used for plasma position. | 25 |
| 3.3 | Schematic drawing of the OH bank system. | 27 |
| 3.4 | Computer rendering of a clamp used to hold and force-load SCRs used in the OH bank system. | 28 |
| 4.1 | Expected induced diamagnetic loop voltage for typical shot. Thin line indicates raw calculations. Thick line is 5 point average of V_p . This calculated signal does not include the influence of noise. | 38 |
| 4.2 | The attenuation of the signal due to the skin effect at the bellows (solid line) and the chamber walls (dotted line) | 42 |
| 4.3 | (a) The primary (single loop) coil and the compensating (non-enclosing) coil located outside the vacuum chamber. (b) The set of auxiliary compensation coils. Although these coils are shown separately for clarity, they are installed coplanar in the same form. | 48 |
| 5.1 | Plasma current, loop voltage, average electron density, and plasma position for a typical normal ohmic discharge. Shot 204760. | 54 |

| | | |
|-----|--|----|
| 5.2 | (a) Plasma, vacuum, and compensated flux signals. (b) Contribution of the toroidal field coils (BT), position feedback system (FB), and ohmic heating coils (OH) to the blank shot baseline. (c) Relative sizes of the feedback and OH contributions to the final compensated shot. Shot 204760. | 55 |
| 5.3 | Measured toroidal flux change, poloidal beta, bulk thermal energy, and energy confinement time. Shot 204760. | 56 |
| 5.4 | Comparison of diamagnetically measured and Spitzer based calculations of poloidal beta. Shot 204760. | 57 |
| 5.5 | (a) Plasma current. (b) Loop Voltage. (c) H_α emission for CT Injection discharge 209987. The dashed line shows a normal ohmic discharge, and the vertical line shows the time of CT injection. | 58 |
| 5.6 | (a) Line averaged electron density. (b) Soft X-Ray emission. (c) Diamagnetically measured poloidal beta. Normal Ohmic (dashed line), Neutral Gas puffing from CT (dotted line), and CT Injection (solid line). The solid vertical line at 17 ms indicates the time of CT injection. Ohmic discharge 210021. Neutral Gas puffing from CT discharge 209985. CT Injection discharge 209987. | 61 |
| 5.7 | Diamagnetic measurement of the plasma bulk kinetic energy for CT Injection shot 209987. | 62 |
| 6.1 | Model depicting the plasma, diamagnetic coil, BT coils, and vacuum chamber as simple circuits with resistance and inductance. | 65 |
| 6.2 | Signal Processing Block Diagram. | 67 |
| 6.3 | Signal Processing Block Diagram. | 67 |
| 6.4 | 50 Ohm Cable driver. | 69 |
| 6.5 | Schematic for amplifiers and signal conditioning circuits for improved diamagnetic measurements. | 70 |
| 6.6 | PCB track layout for improved diamagnetic measurements. | 71 |
| A.1 | Auxiliary (vibrational) compensation coils and primary compensation coils. | 80 |
| A.2 | Coil form with tape strips for coil winding. In this figure, an auxiliary compensation coil is being wound. | 81 |
| A.3 | Coil winding turning corners in the form grooves. A piece of tape is lifted to illustrate the winding method. | 82 |
| A.4 | Diamagnetic coil installed on STOR-M | 83 |
| A.5 | Upper mounting point for Diamagnetic Coil. The mounts are connected to the yokes of the machine, isolating the coil form from the chamber. Lower mount is identical. | 84 |
| A.6 | BNC Breakout box | 86 |
| A.7 | DA 15 pin numbering for male and female connectors | 87 |

LIST OF ABBREVIATIONS

| | |
|--------|--|
| AU | Arbitrary Units |
| CT | Compact Toroid |
| FB | Feed Back |
| MHD | Magneto-Hydrodynamic |
| OH | Ohmic Heating |
| SCR | Silicon Controlled Rectifier |
| STOR-M | Saskatchewan Torus Modified |
| SXR | Soft X-Ray |
| TF | Toroidal Field |
| USCTI | University of Saskatchewan Compact Toroid Injector |

LIST OF SYMBOLS

| | |
|-----------------|-----------------------------------|
| a | Minor Radius |
| B_ϕ, B_T | Toroidal Magnetic Field |
| B_θ | Poloidal Magnetic Field |
| I_θ | Poloidal Current |
| I_p | Plasma Current |
| J | Current Density |
| L_p | Plasma Self Inductance |
| l_i | Plasma Internal Inductance |
| n_e | Electron Density |
| p | Pressure |
| q | Safety Factor |
| r_c | Larmor radius |
| R_o | Major Radius |
| T_e | Electron Temperature |
| V_p | Plasma Loop Voltage |
| v_\perp | Perpendicular Velocity |
| W | Plasma Bulk Thermal Energy |
| α | Gain constant for coil balancing |
| β_θ | Poloidal Beta |
| δ | Skin Depth |
| ΔB_ϕ | Change in Toroidal Magnetic Field |
| $\Delta\Phi$ | Change in Toroidal Magnetic Flux |
| ϵ | Inverse Aspect Ratio |
| ϕ_1 | Enclosing Coil Flux |
| ϕ_2 | Non-Enclosing Coil Flux |
| ϕ_{err} | Residual Flux |
| $\Phi_{\phi e}$ | Externally Applied Toroidal Flux |
| γ | Gain constant for auxiliary coils |
| η_n | Neoclassical Conductivity |
| η_s | Spitzer Conductivity |
| ρ | Mass Density |
| σ | Conductivity |
| τ_c | Vacuum Chamber Time Constant. |
| τ_E | Plasma Energy Confinement Time |
| ω_c | Cyclotron Frequency |

CHAPTER 1

INTRODUCTION

1.1 Motivation

Due to an increasing demand for energy coupled with rising environmental and sustainability issues, the requirement for abundant clean energy is becoming critical. Fusion power offers the world the potential for nearly endless, economically viable energy with a very low environmental footprint [1–3]. It is a leading candidate amongst all forms of alternative energy to meet the world’s rising demands. Continued research on plasma confinement and stability is critical to the goal of achieving fusion power. Diamagnetic measurements provide insight into the energy content of plasma and its confinement time. Plasma energy confinement time is an important parameter to study in experiments examining the control and behavior of magnetically confined plasmas. Diamagnetic measurements provide a direct global measurement of the plasma kinetic pressure.

1.2 Principles of Magnetic Fusion

1.2.1 A Brief History of Fusion

Nuclear fusion has been a topic of intense research since World War II. It has long been thought that the devastating power unleashed in the nuclear weapons of that era could be harnessed for the production of electrical power. Nuclear fission has already been harnessed in this way, providing large amounts of power to many regions of the world. France, for example, relies heavily on nuclear fission power plants for its

energy requirements. Nuclear fusion research hopes to develop economical controlled nuclear fusion and likewise sustain the worlds energy needs. Fusion research has made many large advances over the course of its efforts. Notably, researchers at the JET tokamak demonstrated the production of over a megawatt of fusion power with the release of two mega joules of fusion energy in 1991 [4]. Researchers at JT-60U showed a power gain of 1.25 for D-T equivalent fuel in 1999 [5]. A power gain greater than unity is critical to fusion power plants, as this factor shows that the fusion reaction is producing more power than it takes to sustain it. Indeed, sub-unity power gains have long been a significant problem in fusion devices.

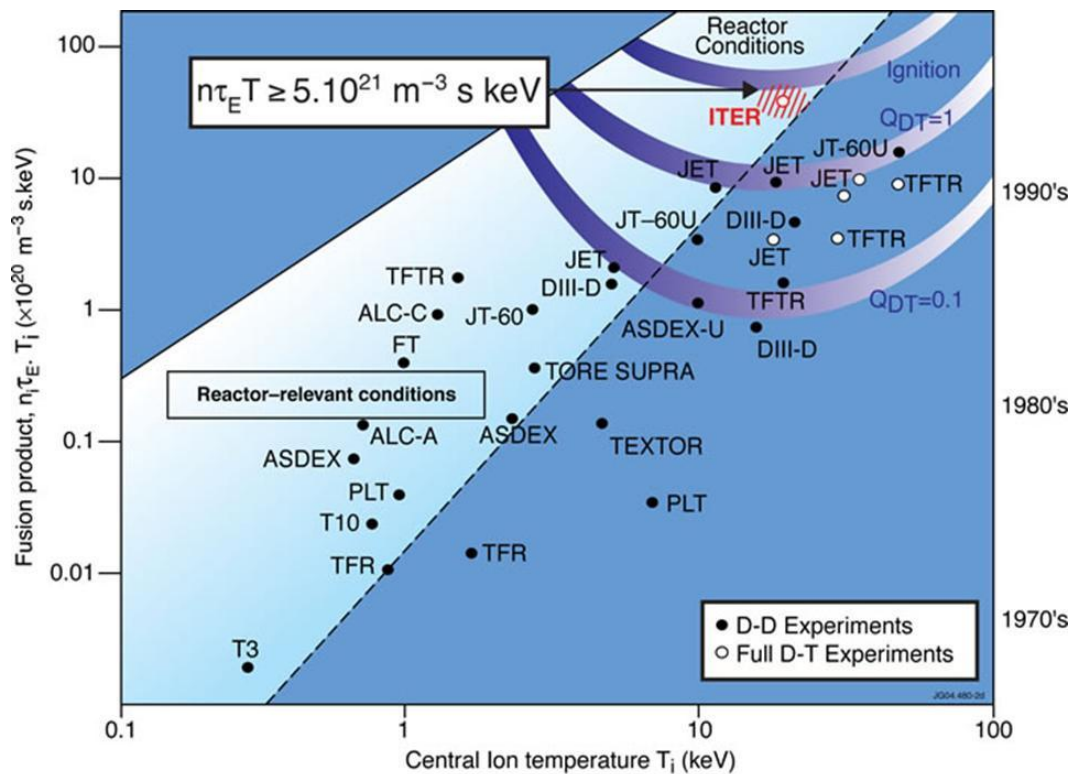


Figure 1.1: Advances in Fusion Research.

However, the fusion research is advancing rapidly. Fig. 1.1 shows that fusion research progresses as rapidly as the development of more complicated microprocessors. Current efforts focus on the development of the ITER tokamak (International Thermonuclear Experimental Reactor) [6,7], which is hoped to provide a bridging step between

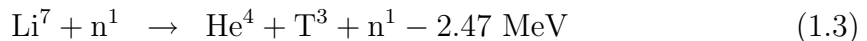
current research and the future of commercial level controlled nuclear fusion power plants. The main objective of ITER is the demonstration of self-sustained burning plasma (primarily through heating by alpha particles). ITER is expected to provide important information about the engineering requirements of fusion reactors, and serve as a test bed for fusion reactor components such as tritium breeding blankets. A proposed American reactor known as the Fusion Ignition Research Experiment (FIRE) [8] is being considered to study advanced tokamak plasmas and alpha dominated heating. The FIRE design describes a compact high field tokamak with cryogenically-cooled copper-alloy coils.

1.2.2 Deuterium-Tritium Reaction

The primary fusion reaction studied in laboratories is the Deuterium-Tritium reaction:



The neutron in the above equation carries 14.1 MeV of the energy released by the reaction. This reaction is chosen because it has the largest cross section, and least demanding conditions ($n \gtrsim 10^{14} \text{ cm}^{-3}$ and $T \gtrsim 10 \text{ keV}$). In a fusion reactor undergoing DT burning, self heating occurs through energy deposition by the alpha particle (He^4). The input fuel Deuterium is readily available from seawater, while Tritium is less easily obtained. Deuterium exists in sea water as heavy water (D_2O) at an abundance of approximately 1 deuterium atom in every 10000 hydrogen atoms [9]. Tritium occurs in natural waters at much lower abundances ranging from 0.5 to 67 tritium atoms per 10^{18} hydrogen atoms [10]. Harvesting of tritium for this reaction is not entirely viable due to the low abundance. Instead, in a fusion device the tritium is typically produced by neutron absorption into installed lithium blankets. This process is often called tritium breeding, and can proceed via the following two reactions [11]:



If equations 1.1 and 1.2 are combined, it is seen that the Deuterium-Tritium reaction is in effect a Deuterium-Lithium reaction:



The neutron bombards the Li^6 isotope of lithium which occurs in an abundance of about 75 atoms in 1000 in natural lithium [12]. Production of tritium through the above equation requires complete utilization of the neutrons produced from the D-T reaction for a sustainable fusion process, otherwise extra tritium needs to be introduced. The lithium blankets installed in the chamber can also be used as heat exchangers to extract energy from the fusion reaction.

1.2.3 Plasmas

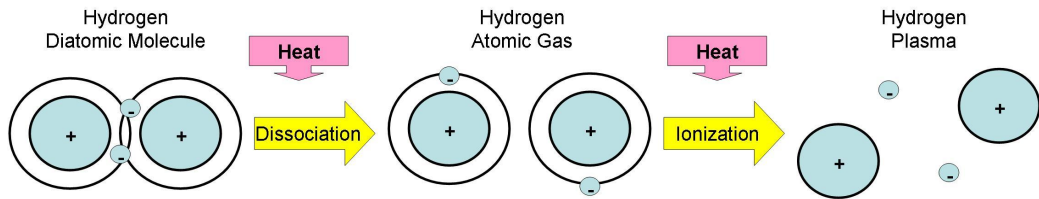


Figure 1.2: Conceptual illustration of matter becoming a plasma. Water begins as a solid (ice) and with heat becomes a liquid, then with further heating becomes a gas. With continued heating, the atoms making up the water molecule disassociate and ionize, becoming plasma.

Plasma is the fourth state of matter, and is generally considered to have the following properties: (1) plasma is a gas containing charged particles, (2) the plasma is quasineutral, (3) the plasma exhibits collective behavior (such as waves). The first condition outlines the transition from gas to plasma; when a gas is energized enough that the neutral particles separate into charged particles (ions and electrons) the gas is said to become a plasma (Fig. 1.2). It is often stated that we live in a universe where 99% of the matter present is in a plasma state, excluding the possibility of dark matter or other unknowns. Conversely, we can state that we occupy a portion of the 1% of the universe where the majority of matter is not in a plasma state.

The plasmas that we do observe are found in the laboratory, in fluorescent and neon lighting, in plasma televisions, in lightning, in the Auroa Borealis, and to some extent in flames. The amount of ionization found in a gas in equilibrium is expressed by the Saha equation [13]:

$$\frac{n_i}{n_n} \approx 2.4 \times 10^{21} \frac{T^{3/2}}{n_i} e^{-U_i/KT} \quad (1.5)$$

where n_i and n_n are the number densities of the ion and neutral species (per m^3), T is the gas temperature in Kelvin, U_i is the ionization energy of the gas, and K is Boltzmann's constant. It is clear from the Saha equation that for standard room temperature and density the fractional ionization is negligible.

The charged particles present in the gas can produce a screening effect. Conceptually, one can consider a single positive charge surrounded by attracted negative charges. In this arrangement, there exists a distance such that the influence of the charges is not felt. This distance is defined to be the Debye length (λ_D) and is given by:

$$\lambda_D^2 = \frac{\varepsilon_0 K T_e}{n e^2} \quad (1.6)$$

Note that the electron temperature is used in this expression. In STOR-M, with typical values of $T_e = 220$ eV and $n \sim 7 \times 10^{12} \text{ cm}^{-3}$ the Debye length is approximately 0.004 mm. Electrons, being less massive than ions are generally more mobile and hence perform the shielding by positioning themselves so as to create the required excess or deficit of negative charge.

If we define the dimensions of a plasma system to be L , and make use of the definition the Debye length, then a convenient description of a plasma is an ionized gas that is dense enough that $\lambda_D \ll L$.

The second condition describes the particle inventory of the plasma, and makes the claim that for a large enough sampled volume the plasma will contain an equal amount of positive and negative charges. In general, quasineutrality allows one to assume the plasma is neutral enough that $n_i \simeq n_e \simeq n$ where n is the plasma density (or common density) but not so neutral that electromagnetic forces are not present. It is these forces that give rise to the third condition: locally arising positive or

negative charge densities give rise to electric fields which can affect that behavior of plasma located at a distance. For collective behavior, it is required that the plasma satisfies the condition $\lambda_D \ll L$ and that the number of particles present in its Debye sphere, N_D :

$$N_D = n \frac{4\pi}{3} \lambda_D^3 \gg 1 \quad (1.7)$$

1.2.4 Plasmas in Magnetic Fields

The electrical properties of plasma, specifically the lack of a strict electrical neutrality, give rise to the ability to magnetically manipulate this highly energetic gas. In fact, magnetic confinement is often necessary for high temperature laboratory plasmas. In order to achieve fusion in the aforementioned D-T reaction, ion temperatures in excess of 7 keV (over 80 million Kelvin) are required. Obviously, gases at these temperatures would destroy any material they come in contact with. Hence, magnetic fields are used to confine the plasmas [14]. Stellarators, Pinches, Mirror Machines, Spheromaks [15], and Tokamaks [16–20] are examples of magnetic confinement devices. Only Tokamaks will be discussed in detail in this work.

Токмак is an acronym derived from the Russian Тороидальная камера в магнитных катушках, pronounced “toroidal’naya kamera v magnitnykh katushkakh,” which literally translates to toroidal chamber in magnetic coils. The basic components of a tokamak are the vacuum chamber, toroidal coils positioned around the chamber, Ohmic heating coils to drive the toroidal plasma current, and vertical field coils to maintain plasma position. Figure 1.3 shows the arrangement of these coils, and the shapes of the field lines produced. It is well known that charged particles will tend to orbit magnetic field lines. The radius of this orbit is known as the Larmor radius (in STOR-M, this radius is on the order of millimeters for ions and micrometers for electrons). The purpose of the toroidal field is to provide confinement by keeping the Larmor radii of the ions small. However, the toroidal field alone does not provide closed magnetic surfaces (necessary for confinement), so the poloidal magnetic field produced by the plasma current is used to produce a net helical field with closed

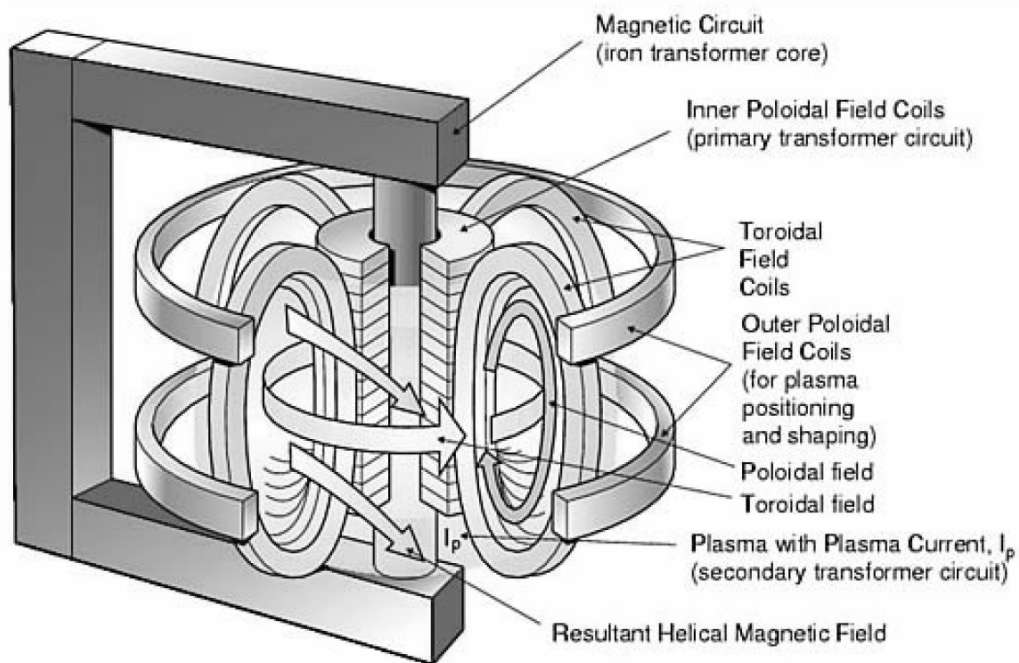


Figure 1.3: Simplified schematic diagram showing the major magnetic components of a tokamak, and the resultant magnetic field. Toroidal field coils, Ohmic heating coils (inner set) and vertical field coils (outer set) can be shown.

magnetic surfaces (layer upon layer of “toruses of flux”). The combination of the toroidal and poloidal field produces a net helical field. The helical field produced can be described in terms of the degree of twisting, or *helicity* through the *safety factor* q [19]:

$$q(\rho) \simeq \frac{\rho B_\phi}{R_o B_\theta(\rho)} \quad (1.8)$$

where ρ is the distance in the minor radial direction, R_o is the major radius, and B_ϕ and B_θ are the toroidal and poloidal magnetic fields, respectively.

In addition to the applied toroidal field, and the produced poloidal field, the tokamak also requires a vertical magnetic field to counter the radial expansion force of the plasma. While the concept of plasma confinement inside a tokamak is simple, the device requires numerous controls to counter the expansion forces and drifts experienced inside the machine. Aside from the vertical field, feedback controls are often employed to maintain plasma position inside the chamber.

1.3 Diamagnetism and Paramagnetism of Plasmas in Tokamaks

Paramagnetic and diamagnetic effects are not separable in tokamak plasmas.

Toroidal plasma current is inclined to flow along the helical field lines inside the tokamak. Current flowing parallel to the helical magnetic field will not contribute to the Lorentz force, and as such is termed *force free current*. Paramagnetism arising from the toroidal current is depicted in Fig 1.4 [21]. From the figure, it is clear that the azimuthal current components add a positive component ($\Delta B_\phi > 0$) to the applied toroidal field, *regardless of the direction of the plasma current*. This effect is well known as the *self-transformer action* of a current carrying plasma in a magnetic field. Literally, a portion of the plasma current is aligned in the same plane as the toroidal field coils, allowing a linkage between the coils as in a transformer.

Plasma paramagnetism can be described through the poloidal component of the plasma current which can be found from the net helical field. If the total field is

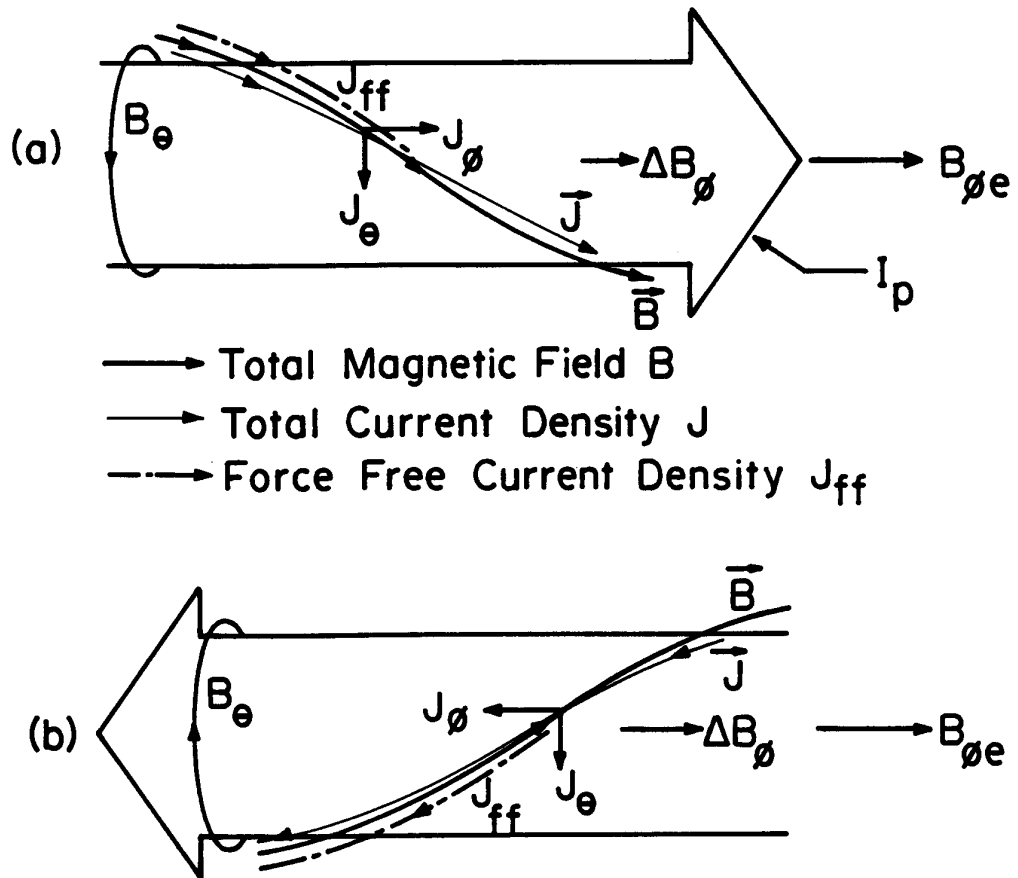


Figure 1.4: Current density components are shown for (a) plasma current flowing with the toroidal magnetic field, and (b) plasma current flowing opposite to the toroidal magnetic field. In both cases, the flux due to J_θ adds to the applied field (paramagnetism).

described in terms of its poloidal and toroidal vector components as

$$\mathbf{B}_{total} = B_\phi \hat{\phi} + B_\theta \hat{\theta} \quad (1.9)$$

and since plasma current is understood to flow along the net helical field, then the poloidal component of plasma current arises from the force-free approximation,

$$J_\theta = \frac{B_\theta}{B_\phi} J_\phi \quad (1.10)$$

The toroidal magnetic field (paramagnetic response, $B_{\phi,p}$) resulting from this poloidal plasma current component can then be calculated from

$$B_{\phi,p} = \left(\frac{B_\theta}{B_\phi} \right) \frac{\mu_0 \int_0^r 2\pi r' j_\phi(r') dr'}{2\pi r} \quad (1.11)$$

if the plasma current profile is known.

In magnetically confined plasmas, a net diamagnetic drift current arises from the magnetic dipole moments associated with the Larmor motion of the ions and electrons. The ion and electron dipole moments are both aligned opposite to the applied magnetic field (toroidal field in tokamaks). The radial pressure gradient inside the chamber is directed such that it decreases from the axis to the edge. The pressure gradient clearly presents an expanding force in the outward radial direction. This pressure gradient also results in an imbalance of particles appearing in the outward radial direction, giving rise to the drift currents. That is, there are more particles in the inner orbits (thick circles) than in the outer. The current interacts with the applied magnetic field giving rise to a force opposing the expansion. In a sense, this diamagnetic current is generated by the plasma to counter the expansion force presented by the pressure gradient.

The connection between diamagnetic flux and the plasma thermal pressure can be examined by considering a single charged particle, e with a mass, m undergoing cyclotron motion with a perpendicular velocity, v_\perp about a magnetic field line B_ϕ . Figure 1.6 [21] illustrates this example. In this preliminary example, the helicity of the magnetic field will be ignored. This particle will have a perpendicular kinetic energy:

$$E_\perp = \frac{1}{2} m v_\perp^2 \quad (1.12)$$

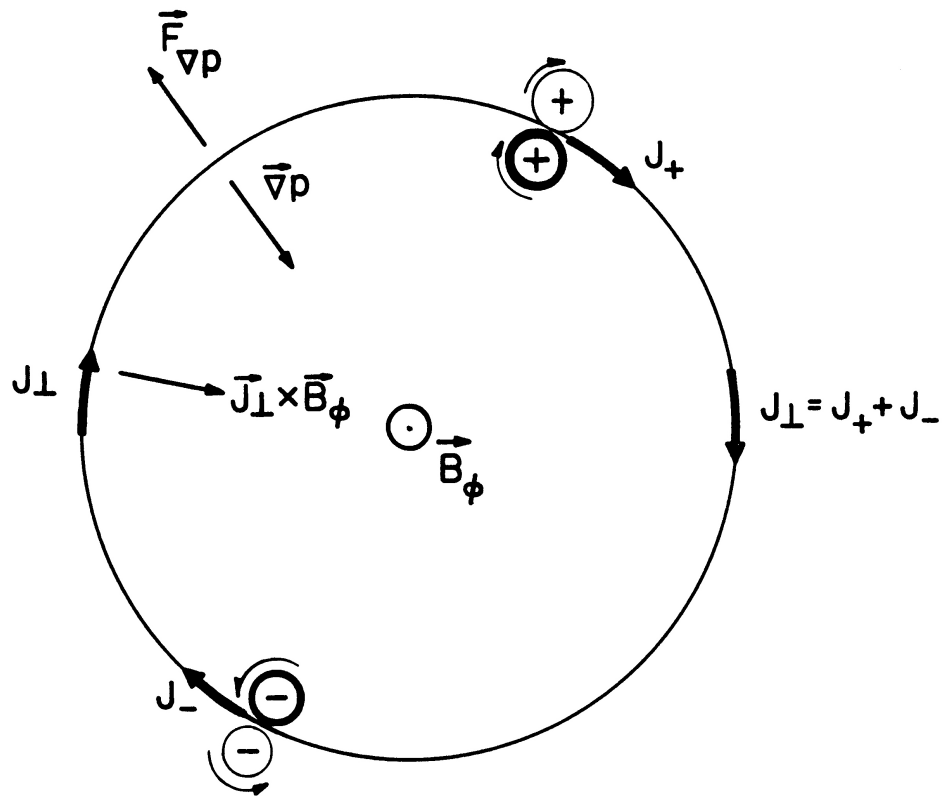


Figure 1.5: Model of plasma diamagnetism showing net current drift J_\perp , plasma pressure gradient ∇p , and expansion force $\mathbf{F}_{\nabla p}$

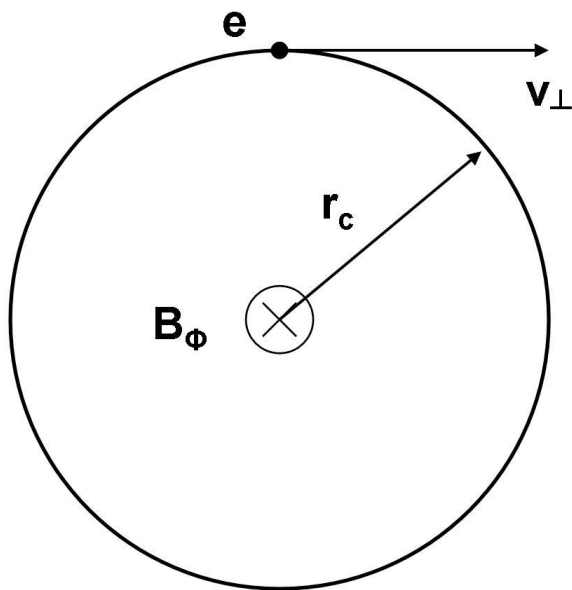


Figure 1.6: A charged particle gyrating about a magnetic field line.

The particle has a current, $I = e/T_c$, where T_c is the period of the cyclotron motion, and encircles an area $A = \pi r_c^2$, where r_c is the radius of gyration. Subsequently, a magnetic dipole moment is produced:

$$\mu_M = IA = \frac{e\pi r_c^2}{T_c} \quad (1.13)$$

Recalling the definitions of the cyclotron frequency and Larmor radius:

$$\omega_c = \frac{e|B|}{m} \quad (1.14)$$

$$r_c = \frac{v_\perp}{\omega_c} \quad (1.15)$$

the magnetic dipole moment can then be written as:

$$\mu_M = -\frac{(e\pi) \left(\frac{v_\perp^2}{\omega_c}\right)}{2\pi/\omega_c} \quad (1.16)$$

$$= -\frac{mv_\perp^2}{2B} \quad (1.17)$$

$$= -E_\perp \frac{1}{B} \quad (1.18)$$

Or, in its vector form as:

$$\mu_{\mathbf{M}} = -\frac{E_{\perp}}{B} \mathbf{b} \quad (1.19)$$

where $\mathbf{b} = \mathbf{B}/B$ is the unit vector in the direction of the magnetic field. Equation 1.19 shows a direct relationship between the magnetic dipole moment and perpendicular kinetic energy of a gyrating particle. A system of charged particles can then be considered as a summation of magnetic dipole moments μ_{M_j} over space, giving the total magnetization \mathbf{M} :

$$\mathbf{M} = -\sum_j n_j \int \mu_{M_j} f_j(\mathbf{v}) d^3v \mathbf{b} \quad (1.20)$$

$$= -\frac{1}{B} \sum_j n_j \int \frac{1}{2} m v_{\perp}^2 f_j(\mathbf{v}) d^3v \mathbf{b} \quad (1.21)$$

where n_j is the density of each species of charged particle j , and $f_j(\mathbf{v})$ is the velocity distribution for that species. If $f_j(\mathbf{v})$ is taken to be Maxwellian, then the integral term can be reduced to the perpendicular temperature:

$$\int \frac{1}{2} m v_{\perp}^2 f_j(\mathbf{v}) d^3v = T_{\perp_j} \quad (1.22)$$

This allows 1.21 to be written as:

$$\mathbf{M} = -\frac{1}{B} \sum_j n_j T_{\perp_j} \mathbf{b} = -\frac{1}{B} \sum_j p_{\perp_j} \mathbf{b} = -\frac{p_{\perp}}{B} \mathbf{b} \quad (1.23)$$

where p_{\perp_j} and p_{\perp} represent the partial and total perpendicular thermal pressures, respectively. It is now possible to express the total magnetic field in terms of the total perpendicular thermal pressure:

$$\mathbf{B} = \mu_0 (\mathbf{H} + \mathbf{M}) \quad (1.24)$$

$$= \mu_0 \left(\mathbf{H} - \frac{p_{\perp}}{B^2} \mathbf{B} \right) \quad (1.25)$$

From equation 1.25 it is clear that the change in the magnetic field due to plasma magnetism ΔB_{ϕ} is given by

$$\Delta B_{\phi} = -\mu_0 \frac{p_{\perp}}{B} \quad (1.26)$$

The change in total magnetic field can be detected experimentally and clearly leads to information regarding the total plasma perpendicular thermal pressure.

When the helical field present in the tokamak is considered, the behavior of the plasma magnetization becomes more complicated. From the safety factor described earlier (equation 1.8), the poloidal magnetic field at the plasma edge can be related to the toroidal magnetic field:

$$B_{\theta} \approx \frac{\varepsilon}{q} B_{\phi} \quad (1.27)$$

where ε is the inverse aspect ratio ($\varepsilon = a/R$). The inverse aspect ratio indicates the toroidicity of the tokamak geometry, and is specific to individual machines (For STOR-M, $\varepsilon \simeq 0.28$) This results in the plasma thermal pressure scaling as:

$$p_{\perp} \propto B_{\theta}^2 \propto I_p^2 \approx \frac{\varepsilon^2}{q^2} B_{\phi}^2 \quad (1.28)$$

The scaling indicates that both the plasma thermal pressure and the poloidal field energy are small compared to the toroidal field energy. This is the underlying challenge in diamagnetic measurements: to extract a very small signal from the midst of a large signal. Chapter two will present a more detailed analysis of plasma diamagnetism based on Magneto-Hydrodynamics (MHD), and chapter four will outline the challenges in obtaining this difficult measurement.

1.4 Thesis Outline

Chapter One has provided the basic background for the work to come in this thesis. Chapter Two deals with the derivation of the measured quantity $\Delta\Phi$ from MHD Equilibrium.

Chapter Three details the STOR-M machine and existing diagnostics used in this work. Various magnetic field systems are discussed, and specific attention is paid to the Compact Toroid injector and the microwave interferometer.

Chapter Four describes the design and construction of the diamagnetic coils. A brief review of diamagnetic measurement techniques is given, and the specific requirements of STOR-M are detailed.

Chapter Five reports on the experimental results obtained. A detailed examination of the residual flux is given, and a comparison is performed between the diamagnetic poloidal beta for normal ohmic discharge data and poloidal beta obtained from measurements of Spitzer temperature. A shot performed with Compact Toroid Injection is presented.

Chapter Six contains the conclusion and a discussion of future work.

CHAPTER 2

MAGNETOHYDRODYNAMIC EQUILIBRIUM

2.1 Equilibrium in the Minor Radial Direction

As previously discussed, the diamagnetic flux is working to balance the radial pressure gradient inside the tokamak. It is therefore necessary to derive equilibrium in the minor radial direction (from chamber center to chamber edge). When examining the equilibrium in the minor radial direction, toroidicity is ignored and the torus is treated as a cylinder (Fig. 2.1). A charge-neutral plasma consisting of ions and electrons is considered. The equations of motion are then

$$Mn_0 \left(\frac{\partial}{\partial t} + \mathbf{v}_i \cdot \nabla \right) \mathbf{v}_i = n_0 e \mathbf{E} + en_0 \mathbf{v}_i \times \mathbf{B} - \nabla p_i \quad (2.1)$$

$$mn_0 \left(\frac{\partial}{\partial t} + \mathbf{v}_e \cdot \nabla \right) \mathbf{v}_e = -n_0 e \mathbf{E} - en_0 \mathbf{v}_e \times \mathbf{B} - \nabla p_e \quad (2.2)$$

where p_i, p_e are the ion and electron pressures, respectively. With the assumptions that these pressures are isotropic, ions are singly charged and considering the electron mass, m is negligible compared to the ions M , therefore writing a mass density $\rho = (M + m)n_0 \simeq Mn_0$, the equations of motion can be summed to produce

$$\rho \left(\frac{\partial}{\partial t} + \mathbf{v} \cdot \nabla \right) \mathbf{v} = \mathbf{J} \times \mathbf{B} - \nabla p \quad (2.3)$$

In this equation the average plasma flow velocity \mathbf{v} is approximated using the ion velocity

$$\mathbf{v} = \frac{M\mathbf{v}_i + m\mathbf{v}_e}{M + m} \quad (2.4)$$

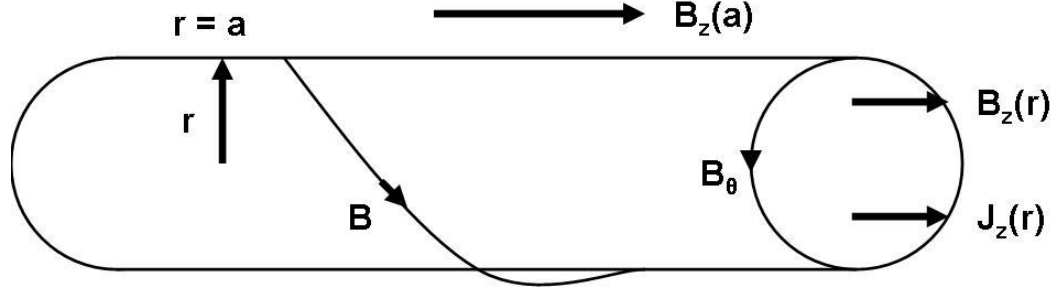


Figure 2.1: The plasma torus is approximated as a cylindrical plasma. The toroidal component is treated as the z axis.

And the current is

$$\mathbf{J} = n_0 e (\mathbf{v}_i - \mathbf{v}_e) \quad (2.5)$$

Considering equation 2.3 at equilibrium ($\frac{\partial}{\partial t} = 0$)

$$\rho \mathbf{v} \cdot \nabla \mathbf{v} = \mathbf{J} \times \mathbf{B} - \nabla p \quad (2.6)$$

Next, the convective term (LHS) can be neglected if the plasma flow velocity is small. Generally in tokamaks the flow velocity is much smaller than the sound speed ($c_s = \sqrt{\frac{p}{\rho}}$), and can therefore be ignored. This is because the flow velocities are dominated by the $\mathbf{E} \times \mathbf{B}$ drift (eq (2.7)) and ion diamagnetic drift (eq (2.8)) velocities. While the electron diamagnetic drift is comparable to the ion diamagnetic drift, it does not contribute to plasma flow due to the small relative mass of the electron.

$$\mathbf{V}_E = \frac{\mathbf{E} \times \mathbf{B}}{B^2} \quad (2.7)$$

$$\mathbf{V}_{*i} = \frac{1}{eB^2} \mathbf{B} \times \nabla p_i \quad (2.8)$$

$$(2.9)$$

$V_{*i} \ll c_s$ is satisfied when the condition that the ion cyclotron radius is much less than the pressure gradient length scale $\rho_i \ll L_p$. This condition is trivially satis-

fied in any practical confinement device, since if it was not, the ions would hit the chamber walls and there would not be confinement. However, in an axisymmetric confinement device (such as a tokamak), the assumption $V_E \ll c_s$ is not always true when considering the toroidal $\mathbf{E} \times \mathbf{B}$ drift

$$V_\phi = -\frac{E_r}{B_\theta} \quad (2.10)$$

V_ϕ may approach the sound velocity near the edge of a confined plasma.

Considering the flow velocity as negligible, the equation of MHD equilibrium becomes

$$\nabla p = \mathbf{J} \times \mathbf{B} \quad (2.11)$$

Using Ampere's law

$$\nabla \times \mathbf{B} = \mu_0 \mathbf{J} \quad (2.12)$$

Eq. (2.11) can be rewritten as

$$\nabla \left(p + \frac{B^2}{2\mu_0} \right) = \frac{1}{\mu_0} \mathbf{B} \cdot \nabla \mathbf{B} \quad (2.13)$$

Considering the radial component of Eq. (2.13), and noting the curvature term $(\mathbf{B} \cdot \nabla \mathbf{B})_r = -\frac{B_\theta^2}{r}$ (B_z is assumed to be straight), the previous equation then leads to

$$\frac{\partial}{\partial r} \left(p + \frac{B_\theta^2}{2\mu_0} + \frac{B_z^2}{2\mu_0} \right) = -\frac{1}{\mu_0} \frac{B_\theta^2}{r} \quad (2.14)$$

Eq. (2.14) can be rearranged as

$$\frac{\partial}{\partial r} \left(p + \frac{B_z^2}{2\mu_0} \right) = -\frac{1}{2\mu_0} \frac{1}{r^2} \frac{\partial}{\partial r} (rB_\theta)^2 \quad (2.15)$$

If this equation is multiplied by r^2 , it can be integrated from the axis to the plasma edge ($r = 0$ to $r = a$), obtaining the basic equilibrium equation

$$\bar{p} + \frac{1}{2\mu_0} \left[\overline{B_\phi^2} - B_\phi^2(a) \right] = \frac{1}{2\mu_0} B_\theta^2(a) \quad (2.16)$$

where \bar{p} and $\overline{B_z^2}$ are averages across the plasma cross section

$$\bar{p} = \frac{1}{\pi a^2} \int_0^a 2\pi p(r) r dr \quad (2.17)$$

$$\overline{B_z^2} = \frac{1}{\pi a^2} \int_0^a 2\pi B_z^2(r) r dr \quad (2.18)$$

The poloidal beta β_θ , is defined as the ratio of the volume averaged plasma thermal pressure and poloidal magnetic field energy density

$$\beta_\theta = \frac{\langle nT \rangle}{B_\theta^2(a)/2\mu_0} \quad (2.19)$$

From basic equilibrium (Eq. (2.16)), the change in toroidal magnetic energy density is given by

$$\frac{1}{2\mu_0} \left(\overline{B_\phi^2} - B_\phi^2(a) \right) = \frac{B_\theta^2}{2\mu_0} (1 - \beta_\theta) \quad (2.20)$$

where

$$\beta_\theta = \frac{2\mu_0}{B_\theta^2(a)} \overline{p} \quad (2.21)$$

The change in flux, from both diamagnetism and paramagnetism (arising from self-transformer action) is given as

$$\Delta\Phi_p = (\overline{B_\phi} - B_\phi(a)) \pi a^2 \quad (2.22)$$

where

$$\overline{B_\phi} \equiv \sqrt{\overline{B_\phi^2}} \quad (2.23)$$

The poloidal beta quantity can be calculated from

$$\beta_\theta = 1 - \frac{8\pi B_\phi(a)}{(\mu_0 I_p)^2} \Delta\Phi_p \quad (2.24)$$

where $B_\phi(a)$ is the toroidal magnetic field, I_p is the plasma current, and $\Delta\Phi_p$ is measured change in toroidal magnetic flux. The plasma is considered diamagnetic for values of $\beta_\theta > 1$ [22]. Values below 1 indicated paramagnetism (where the produced field supplements the applied field).

The ratio of the plasma diamagnetic flux to the total flux is given as

$$\frac{\Delta\Phi_m}{\Phi_{\phi_e}} = \frac{1}{2} \frac{B_\theta^2(a)}{B_\phi^2} (1 - \beta_\theta) \quad (2.25)$$

with the poloidal magnetic field evaluated at the edge of the plasma

$$B_\theta(a) = \frac{\mu_0 I_p}{2\pi a} \quad (2.26)$$

2.2 Bulk Plasma Thermal Energy and the Energy Confinement Time

The energy confinement time of a plasma is a term often misunderstood. It has nothing to do with the discharge duration, but is a statement of the rate energy is lost from the system. The confinement time, τ_E is a measurement of the ratio of the thermal energy contained in a plasma and the amount of input energy required to maintain the conditions in the plasma (alternatively, the amount of energy lost from the system without input). Confinement time increases with volume, as larger volumes of plasma show improved heat retention.

The bulk plasma thermal energy can be found from the volume averaged kinetic pressure, which can be found by measuring the poloidal beta quantity and the plasma current:

$$\langle p \rangle = \frac{B_\theta^2(a)}{2\mu_0} \beta_\theta = \frac{\mu_0 I_p^2}{8\pi^2 a^2} \beta_\theta \quad (2.27)$$

If the plasma pressure is considered in terms of the thermal energy density:

$$p = \sum n_j T_j = \frac{2}{3} \sum E_{Tj} = \frac{2}{3} E_T \quad (2.28)$$

then the bulk plasma thermal energy can be expressed in terms of the volume of the toroidal plasma ($V = 2\pi^2 a^2 R$) and the volume averaged kinetic pressure:

$$W = \langle E_T \rangle V = \frac{3}{2} \langle p \rangle V \quad (2.29)$$

With knowledge of the bulk plasma thermal energy, the confinement time can then be calculated. For a tokamak plasma not undergoing fusion, the rate of energy loss is expressed as:

$$\frac{dW}{dt} = P_{in} - P_{out} \quad (2.30)$$

where P_{in} represents the input power, and P_{out} represents the power lost.

The rate of energy loss in an ohmically heated plasma can be described by:

$$\tau_E = \frac{W}{P_{out}} \quad (2.31)$$

while the input power from ohmic heating is given by

$$P_{in} = I_p V_{rp} \quad (2.32)$$

where V_{rp} is the resistive portion of the plasma loop voltage, which can be found by correcting the measured loop voltage for plasma inductance:

$$V_{pr} = V_p - \frac{d}{dt} (L_p I_p) \quad (2.33)$$

where L_p is the plasma self inductance. The plasma self inductance can itself be calculated from

$$L_p = \mu_0 R_0 \left[\ln \left(\frac{8R}{a} \right) - 2 + \frac{l_i}{2} \right] \quad (2.34)$$

where l_i is the plasma internal inductance parameter, found from

$$l_i \equiv \frac{2\pi \int_0^a B_\theta^2 \rho d\rho}{\pi a^2 B_\theta^2(a)} \quad (2.35)$$

which is calculated to be $l_i = 0.92$ for STOR-M, and often approximated as $l_i = 1$. For STOR-M, a parabolic current profile was assumed

$$j = j_0 \left(1 - \frac{\rho^2}{a^2} \right) \quad (2.36)$$

Substitution of Eq. 2.31 and 2.32 into Eq. 2.30, with use of Eq. 2.33 yields the energy confinement time in terms of measurable quantities,

$$\tau_E(t) = \frac{3}{8} \mu_0 R_0 I_p(t) \frac{\beta_\theta(t)}{V_p(t) - \frac{d}{dt} (L_p I_p(t))} \quad (2.37)$$

CHAPTER 3

MACHINE DESCRIPTION

3.1 STOR-M Tokamak

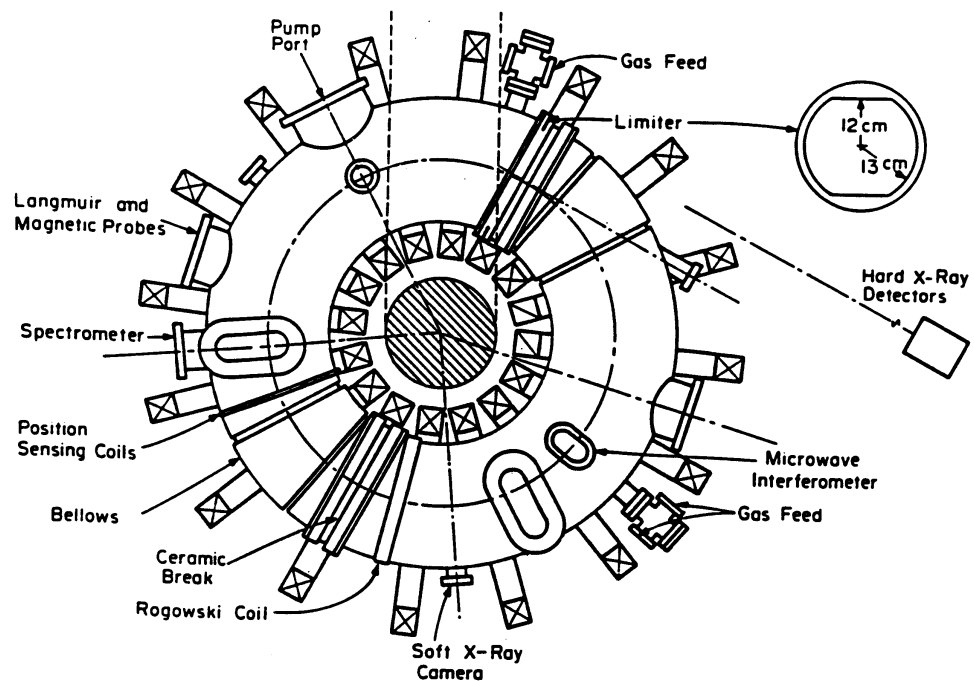


Figure 3.1: Overhead sketch of the STOR-M Tokamak showing diagnostics. Insert shows limiter cross section.

STOR-M is an acronym for Saskatchewan Torus Modified. It is a tokamak housed at the Plasma Physics Laboratory at the University of Saskatchewan. STOR-M was constructed in 1987 to replace the STOR-1M tokamak (major radius $R = 22$ cm,

minor radius $a = 3.5$ cm). Both tokamaks were conceived with Turbulent Heating (TH) experiments, studies of H-mode transitions, and AC operation experiments in mind. The larger size of STOR-M (compared with STOR-1M) is intended to allow clearer studies in the preferential edge heating associated with the skin effect during turbulent hearing, and to be less susceptible to impurity problems. STOR-M is also used for studying fueling by Compact Toroid Injection.

By design, the STOR-M tokamak is easy to reconfigure, which allows it to serve as a test bed for numerous experiments that would be more difficult to perform on larger machines. Recently, STOR-M was configured to simulate start up conditions in a spheromak [23]. STOR-M has also performed numerous experiments in AC operation [24], Turbulent Heating Operation [25], Plasma Biasing [26,27], Compact Toroid Injection Fueling [28], MHD and density fluctuations [29, 30], and Plasma Flow measurements [31,32]. The parameters of STOR-M are listed in table 3.1 [33], and an overhead view is presented in Figure 3.1.

| | | |
|--------------------------|----------|---|
| Major radius | R | 46 cm |
| Minor radius (limiter) | a | 12 cm |
| Toroidal B field | B_ϕ | 1 T |
| Plasma current | I_p | 30-50 kA |
| Average electron density | n_e | $1 \sim 3 \times 10^{13} \text{ cm}^{-3}$ |
| Electron temperature | T_e | 220 eV |
| Ion temperature | T_i | 50 \sim 100 eV |
| Discharge duration | t_d | 50 ms |
| Energy confinement time | τ_E | 1 \sim 3 ms |

Table 3.1: STOR-M Parameters

3.2 Vacuum Chamber and Gas Feed Systems

The vacuum chamber for the STOR-M was created from a pair of stainless steel pipe elbows (circular cross-section) to which a variety of ports have been affixed. The

stainless steel is type 304L, with a thickness of 4 mm [34]. Each of the elbows forms one half of the chamber. The elbows are connected to a flexible bellows section to relieve mechanical stress. The thickness of the bellows section is 0.5 mm. Ceramic breaks are used to interrupt toroidal currents that would otherwise be induced in the chamber structure by the Ohmic Heating (OH) coils. A stainless steel limiter (also type 304L) determines the minor radius of the plasma. The limiter consists of two vertical circular limiters and a pair of horizontal rail limiters (see inset, Figure 3.1. The limiter sets the minor radius of the plasma at 12.5 cm and allows for up to 1 cm of additional horizontal movement without further scrape-off.

Vacuum pumping is provided by a 1000 L/sec turbo molecular pump (TMP) system with a rotary vane roughing pump [35, 36]. Additional pumping is provided by the 450 L/sec TMP mounted on the Compact Torus Injector. Typically, the chamber reaches a base pressure of $1 - 2 \times 10^{-7}$ Torr, although pressures as low as 2×10^{-8} Torr have been obtained with the use of chamber baking. For plasma discharges, the chamber is filled to roughly 1×10^{-4} Torr with ultra-pure hydrogen (99.999%). This “steady fill” is achieved with a Veeco Automatic Pressure Controller [37] operating a Veeco PV-10 piezoelectric gas valve [38]. During the discharge, a programmable gas puffing system is used to increase plasma density (both for plasma quality, and to disrupt the discharge at a desired time). Gas puffing occurs through two MaxTek MV-112 valves (replacements for the PV-10 valves).

3.3 Magnetic Field Systems

STOR-M uses a set of toroidal field coils to produce the toroidal magnetic field. Poloidal coils are used to drive ohmic current used for plasma production, heating (Joule heating process), and confinement. Vertical field coils provide the necessary magnetic field to obtain equilibrium in the major radial direction. Figure 3.2 shows the locations of the primary coils on STOR-M. The primary magnetic field systems on STOR-M will be briefly summarized.

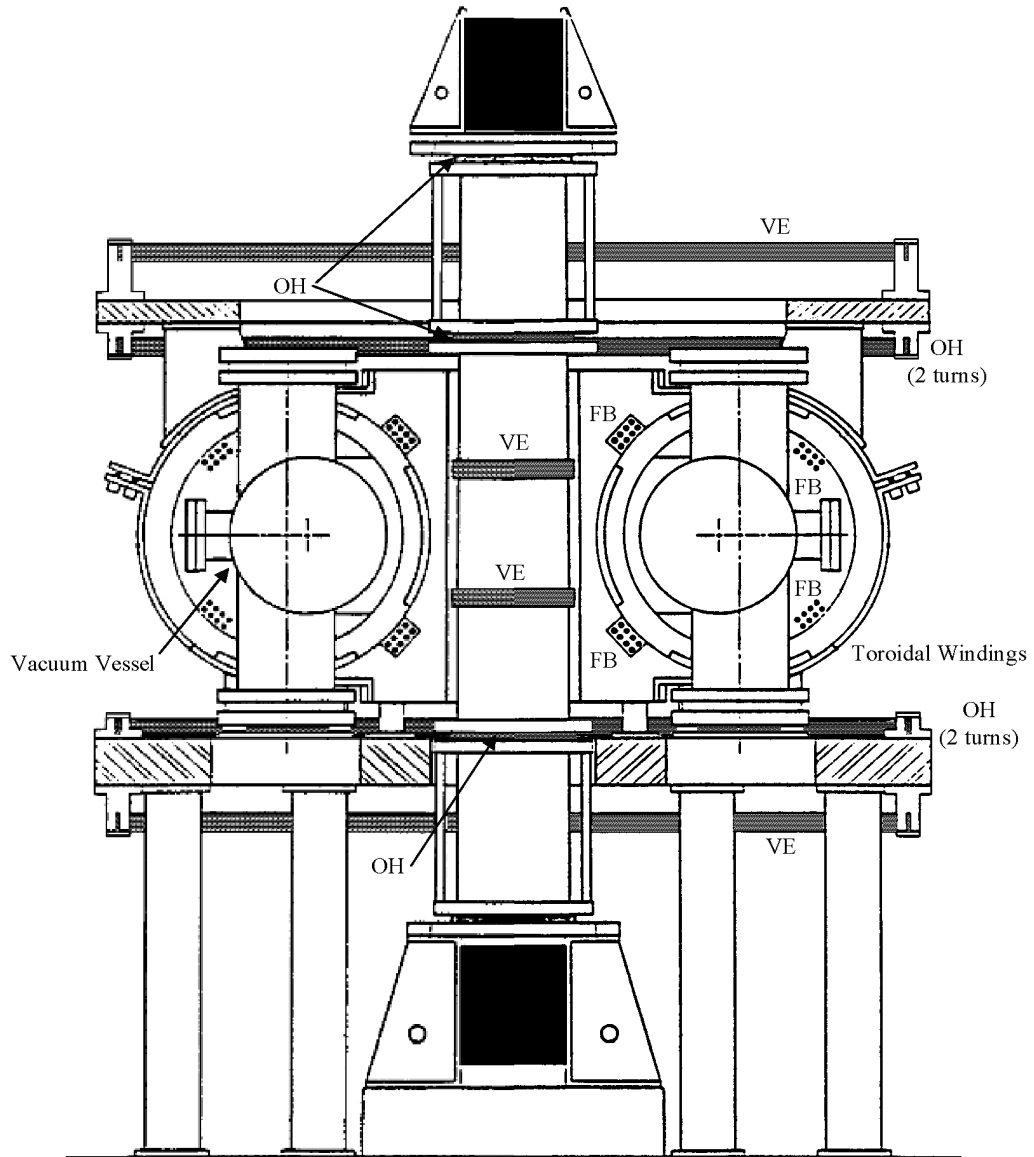


Figure 3.2: Vertical cross section scale diagram of the STOR-M Tokamak showing magnetic coils. OH refers to the ohmic heating coils used for heating. VE refers to the vertical field coils used to obtain equilibrium. FB refers to the feed back coils used for plasma position.

3.3.1 Toroidal Field System

There are 16 uniformly spaced circular coils that make up the toroidal field system on STOR-M. Each coil contains 9 turns of copper conductor with a cross-section of 70 mm by 6.4 mm. The windings are concentric, and separated by mylar for insulation. Layers of fiberglass epoxy are used for reinforcement, and each coil is housed in a stainless steel case. A steel belt (1.3 cm thick) is used to compress the coils against the center support structure, providing stability against the large compressive and torsional forces that act on the coil during discharges. The coil support structures ultimately connect to the large phenolic yoke of the tokamak.

The toroidal coils are connected in a series arrangement resulting in 144 turns with a total resistance of 13.5 m Ω at room temperature and a total inductance of 2.06 mH. The series connection is made at the lower outboard side of the toroidal field coils. The feeding busbar has a return line that runs back along the circumference of the machine. The close pairing of the send and return current paths helps limit the magnetic influence of the feeding current. The coils are powered by a capacitor bank consisting of 22 capacitors. The complete bank is rated for 15 mF, 7 kV and can store a maximum of 360 kJ of energy. The capacitors are connected to the coils through an Ignitron and are in parallel with a passive crowbar diode. The rise time of the toroidal field current is approximately 6.5 ms, while the decay time is approximately 400 ms.

Due to the capacitive discharge driving the toroidal field system, the toroidal field produced in STOR-M is not constant. The field decays by approximately 20% over a 50 ms discharge. The presence of the decaying field causes additional challenges in diamagnetic measurements in STOR-M, which will be outlined later.

3.3.2 Poloidal Field System

Poloidal coils on STOR-M provide ohmic current drive and heating. 3 capacitor banks are used to energize the poloidal coils. A bias bank (450 V, 200 mF) establishes a magnetic bias flux in the system. A fast bank (450 V, 200 mF) provides a rapid

initial energy transfer during ramp up, and a slow bank (100 V, 10 F) provides heating over the duration of the pulse. The arrangement of these banks is shown in Fig. 3.3.

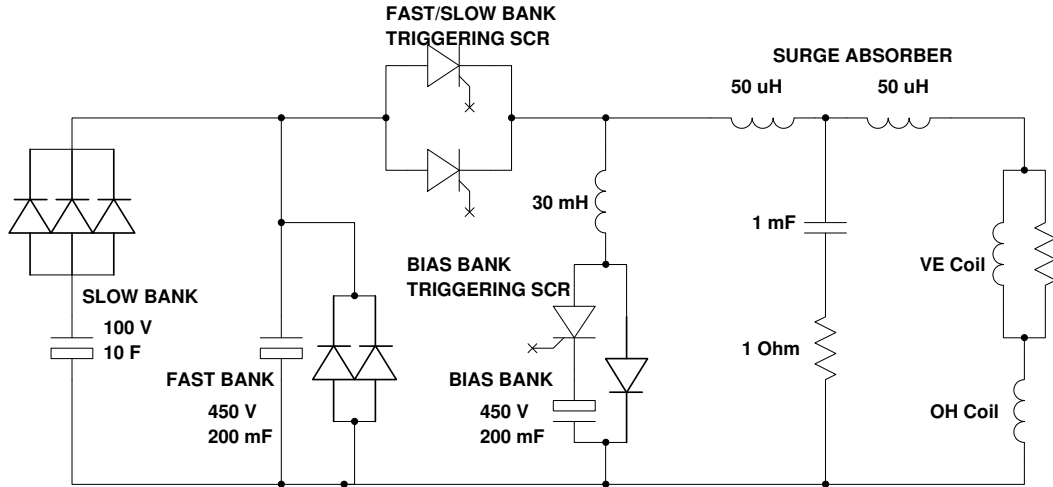


Figure 3.3: Schematic drawing of the OH bank system.

The initial design of the triggering system for the OH banks used a pair of matched Powerx (TA20, 1800 A) SCRs [39]. Work is underway to replace these SCRs with a single unit built by ABB semiconductors [40]. The SCRs are operated under a loading force provided by a clamping mechanism (Fig. 3.4). The banks have also been fired through an ignitron, GL 5551 [41]. The greater voltage drop across the ignitron makes it less desirable than an SCR, however it is much more tolerant of voltage and current spikes.

3.3.3 Position Feedback Control System

The plasma position during STOR-M discharges is controlled by an automatic position feedback control system [12, 42]. It is important that the position of the plasma column is well controlled to maintain high quality plasma discharges. The earlier analog PID system was modified to a fuzzy logic system including digital control and an Arbitrary Signal Generator to achieve improved control [42]. The fuzzy logic system does not rely on a system model, better suiting this method to plasma con-

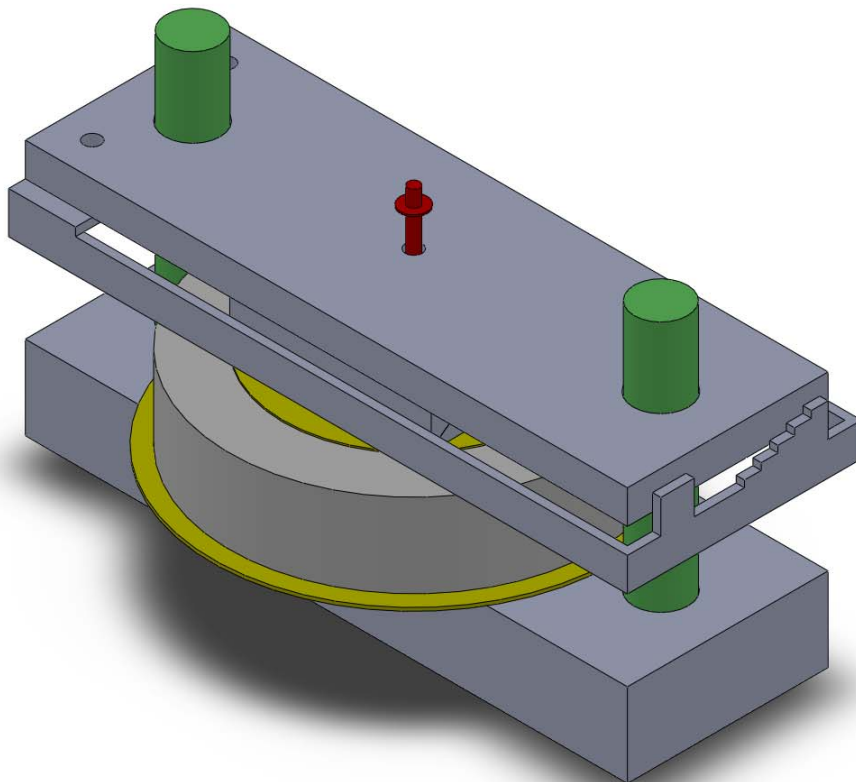


Figure 3.4: Computer rendering of a clamp used to hold and force-load SCRs used in the OH bank system.

trol. An accurate system model is difficult to achieve due to the highly nonlinear and time varying properties of the tokamak discharge. It was found that the digital system was easier to optimize than the analog system. Control fields are applied to the plasma by a several bundles of cables winding along the torus. Magnetic sensors placed around the poloidal direction provide input information about the position of the plasma column.

3.4 Compact Toroid Injection System

Compact toroid (CT) injectors are experimental fueling methods for tokamaks [43–46]. The CT injector is a coaxial plasma accelerator which can deliver fuel to the center of the tokamak.

The University of Saskatchewan Compact Toroid Injector (USCTI) [47] is currently in operation for fueling experiments with STOR-M. The USCTI energizes pure hydrogen in a formation stage where a large capacitor bank is used to break down the gas. Following breakdown, a second large capacitor bank fires to provide the energy for accelerating the CT into the tokamak. The compact torus is compressed from a radius of 7.4 cm to a radius of 5 cm during the acceleration stage. A set of magnetic probes along the length of the CT injector give information about the formation, acceleration, and quality of the CT. There are two sets of quartz windows to allow the use of a He-Ne interferometer.

By tuning the acceleration, the CT can be deposited at a chosen position in the tokamak (radial direction for tangential injection). Table 3.2 [47] lists the typical parameters of the CT exiting the accelerator. CT fueling has been shown to induce improved confinement modes in STOR-M [28].

3.5 Soft X-Ray

The Soft X-Ray (SXR) diagnostics on STOR-M consists of two miniature pin-hole cameras [48]. Each camera contains an array of 12 photodiodes (IRD AXUV-20EL).

| | |
|----------------------|---------------------------------------|
| Radius | 5 cm |
| Length | ≈ 15 cm |
| Density | $1 - 4 \times 10^{21} \text{ m}^{-3}$ |
| Electron Temperature | ≤ 10 eV |
| Magnetic Field | ≈ 0.2 T |
| Velocity | $\leq 150 - 200$ km/s |
| Mass | $\leq 1 \mu\text{g}$ (Hydrogen gas) |

Table 3.2: USCTI Parameters

The cameras collect SXR emission allowing 12 fan-like lines of sight across the plasma bulk. The light collected by the camera diodes is filtered to remove the visible spectrum by $1.8 \mu\text{m}$ (or $7.5 \mu\text{m Be}$) foil. Both cameras are mounted at the same toroidal location, but one is mounted vertically and one is mounted horizontally.

3.6 Interferometer

The STOR-M tokamak is equipped with a 4 mm microwave interferometer. Such interferometer systems are standard diagnostics on tokamaks [49]. The system on STOR-M uses a reflex klystron operating at 75 GHz ($\lambda = 4$ mm) to provide microwaves which are shared amongst a plasma path and two reference paths. The plasma path introduces a phase shift ($\Delta\Phi_\mu$) due to differing indices of refraction. The phase shift is what provides the means to calculate the plasma density from

$$\Delta\Phi_\mu = \frac{2\pi}{\lambda} \int_{-a}^a \left(1 - \sqrt{1 - \frac{n_e(x)}{n_c}} \right) dx \quad (3.1)$$

where $n_e(x)$ is the local electron density, and n_c is the cutoff electron density for the given microwave frequency

$$n_c = \frac{m\epsilon_0\omega^2}{e^2} \quad (3.2)$$

For a 4 mm wave, the cutoff density is $7 \times 10^{19} \text{ m}^{-3}$. This value is an upper limit for density measurements in STOR-M. Physically, the microwave path is fixed in a single horizontal position. As well, $n_e(x)$ and $\Delta\Phi_\mu$ are related quantities, so the central line-averaged electron density is the actual quantity measured

$$\bar{n}_e = \frac{1}{2a} \int_{-a}^a n_e(x) dx \quad (3.3)$$

Upon exiting the tokamak chamber, the plasma microwave signal is then split into two waves E_{s1} and E_{s2} after passing through an E-H tuner. The reference waves E_{r1} and E_{r2} are mixed with the plasma signal in hybrid tees after being attenuated and phase shifted. Silicon point-contact diodes (Alpha industries 1N53) are used to detect the microwaves. Buffer amplifiers accept the diode signals and adjust their gains to compensate for differences in diode efficiencies. The output of the buffer amplifiers is then given as

$$V_{1,2} = K_{1,2} \cos \theta_{1,2} \quad (3.4)$$

where $\theta_{1,2}$ are the phase angles of the microwaves. Correctly adjusting the phase shifts yields

$$V_1 = K_1 \sin \Delta\Phi_\mu \quad (3.5)$$

$$V_2 = K_2 \cos \Delta\Phi_\mu \quad (3.6)$$

This output can be read in real-time by a fringe counting circuit [50], or can be analyzed in post-processing by a zero crossing algorithm to yield the line averaged density.

3.7 Rogowski Coils and Voltage Loop

A Rogowski coil is a toroidal coil typically used to measure current. The coil consists of N number of turns wound around a non-magnetic toroidal former. The coil is

placed around a conductor carrying a time-varying current. The varying current induces a voltage in the Rogowski coil that is proportional to the number of turns N in the coil and the time derivative of the magnetic flux ϕ linked to the coil,

$$V_{RC} = -N \frac{d\phi}{dt} \quad (3.7)$$

Integration of V_{RC} yields the magnetic flux as a function of time. The current in the conductor enclosed by the Rogowski coil can be obtained from Ampere's law

$$I = \oint_c \vec{H} \cdot d\vec{l} \quad (3.8)$$

$$= \frac{1}{\mu_0} \frac{\phi}{a_{RC}} b_{RC} 2\pi R_{RC} \quad (3.9)$$

$$= -\frac{2\pi R_{RC}}{\mu_0 N a_{RC} b_{RC}} \int V_{RC} dt \quad (3.10)$$

where R_{RC} is the coil major radius, a_R is the coil width, and b_{RC} is the coil thickness. The Rogowski coils on STOR-M are typically wound from 26 AWG enameled wire. The notable exception is the coil used for monitoring plasma current, which is wound from 18 AWG wire. The forms are toroidal with rectangular cross-sections. Integration of coil signals is performed by gated, active electronics in the STOR-M control room. The coils signals are transferred via RG 58/U cable. STOR-M's Rogowski coils have a linear frequency response up to 800 kHz.

The plasma loop voltage is monitored with a wire wound along the chamber in the toroidal direction, parallel to the plasma. Measurements plasma loop voltage and plasma current are important in characterizing the discharge, and in estimating the plasma resistivity.

3.8 Spitzer Temperature

The poloidal beta term is calculated from measurements of the line averaged density made using the 4 mm microwave interferometer, and estimate of the electron temperature made using the neoclassical resistivity [51]

$$\eta_n = \frac{\eta_s}{1 - 1.95\sqrt{\epsilon} + 0.95\epsilon} \quad (3.11)$$

where ϵ is the inverse aspect ratio of the tokamak ($\epsilon = \frac{a}{R}$), and η_s is the well known Spitzer resistivity [52]. Spitzer-neoclassical resistivity has been previously confirmed in Zarnstorff *et al* [53]. It was shown in TFTR from direct measurements of electron temperature by Thompson scattering diagnostics and by theoretical calculations that corrections for toroidally trapped particles (neoclassical conductivity) is necessary. Temperature is found through measurements of resistivity. The Spitzer conductivity [54] is given as:

$$\sigma = 1.9 \times 10^4 \frac{T_e^{3/2}}{Z_\sigma \ln \Lambda} [\Omega^{-1}\text{m}^{-1}] \quad (3.12)$$

where T_e is the electron temperature in electron volts, Z_σ is an adjustment for impurities ($Z_\sigma = 1$ for pure hydrogen, $Z_\sigma = 1.5$ assumed for STOR-M), and $\ln \Lambda$ is the Coulomb logarithm. The Coulomb logarithm can be taken as a constant, with an assumed value between 15 and 17. In order to obtain the temperature from the Spitzer conductivity, the plasma resistivity is found.

The plasma loop voltage [12] is given as:

$$v_l = I_p R_p + \frac{d}{dt} [L_{11}I_1 + L_{12}I_2] + \dot{\phi}_{13} + \dot{\phi}_{14} + \dot{\phi}_{15} \quad (3.13)$$

During equilibrium, this equation simplifies:

$$V_l - \frac{d}{dt} (L_p I_p) = I_p R_p \quad (3.14)$$

$$R_p = \frac{V_l - \frac{d}{dt} (L_p I_p)}{I_p} \quad (3.15)$$

where L_p is the plasma loop inductance. The resistance of the plasma can readily be obtained from the measured loop voltage, V_l and plasma current I_p . The plasma resistance is also expressed in terms of the plasma resistivity as:

$$R_p = \frac{2\pi R}{\pi a^2} \eta_{||} \quad (3.16)$$

where η_{\parallel} is the plasma parallel resistivity (assumed to be neoclassical resistivity). The plasma resistivity in STOR-M is similar to that of copper (order of magnitude similarity). In this way, plasma resistivity can be measured, allowing for temperature to be calculated. It is assumed that $T_i = \frac{1}{3}T_e$ (generally reasonable, based on experimental data), and that Z_{σ} is a constant value of 1.5. It is likely that Z_{σ} shows some variation during the breakdown and current ramp up phase of the discharge [55], and the value of 1.5 needs verification. It is not likely that Z_{σ} varies outside of the range of 1.2 to 1.7 in the STOR-M tokamak, and therefore Spitzer calculations are affected by less than 10% by this assumption.

CHAPTER 4

EXPERIMENTAL CONFIGURATION

4.1 Methods of Diamagnetic Measurements

A brief review of diamagnetic measurements is provided, followed by a detailed description of the STOR-M diamagnetic coils.

4.1.1 Measurement of Toroidal Feed Lines

In some situations, the toroidal field coils surrounding the vacuum vessel can be used to measure the diamagnetic current. Diamagnetic currents in the plasma will induce a current in these surrounding coils, which appears as a small change in the applied current. A Rogowski coil placed on the toroidal field current feed line can measure this change in current. This method has advantages in that it is incredibly simple (although it requires a high degree of common mode rejection), and utilizes a large number of coils sampling around the torus. The poloidal beta can be obtained from this method by use of equation 2.24 and the condition of flux conservation (see section 3.7)

$$N\Delta\Phi + L\Delta I = 0 \tag{4.1}$$

where ΔI is the change in current (due to plasma diamagnetism/paramagnetism) measured in the toroidal field feed line. ΔI is taken positive for induced currents in the same direction as the applied toroidal field current. Combining these equations yields

$$\beta_{\theta} = 1 + \frac{L}{N} \frac{8\pi B_T}{\mu_0^2 I_p^2} \Delta I \quad (4.2)$$

The measurement obtained is an average around the torus (due to the measurement being taken consisting of contributions from each TF coil). This method can suffer from reduced sensitivity, as well as noise problems from the feed lines. However, the simplicity of this method has made this approach desirable on occasion. For example, if the applied toroidal field current is constant then a Rogowski coil placed upon the toroidal feed line will measure only the diamagnetic/paramagnetic signal which varies with time. STOR-1 utilized this method [56]. Variations of the method of obtaining the diamagnetic signal from measurements of the toroidal feed line current have been reported on several machines [57–59].

4.1.2 Method of Compensated loops

A very common method is to use compensated loops. This is the method outlined in this thesis. In essence, a single loop is placed around the plasma column to capture the total toroidal flux. Another loop which does not enclose the plasma column is used to measure the background toroidal flux. Additional loops are sometimes used to make fine corrections, or for the elimination of signals due to vibration. The loop systems are either located inside the vacuum chamber [60–63], or are mounted outside of the chamber [64–71]. Papers describing external mounting arrangements usually include additional compensation to correct for the influence of the conducting chamber. Superconducting machines with constant toroidal fields can perform diamagnetic measurements without a compensating loop [72, 73]. A pair of concentric loops can be used to extract the diamagnetic signal from the differential signal between them [74], provided a large enough separation can be achieved. The diamagnetic signal is then sometimes used as input for plasma position feedback controls [75, 76].

4.1.3 Method employed on STOR-1M

Diamagnetic flux measurements were successfully performed on STOR-1M [21]. The system consisted of a single loop primary coil for the flux measurement, a multi-turn primary compensating coil to correct for stray flux, and a pair of multi-turn auxiliary compensation coils to correct for vibrational effects. The STOR-1M diagnostics used a passive mixing circuit with an amplification stage on the final output to provide a signal for post processing via mainframe computer; it was not real time diagnostics. The post processing option was chosen to avoid the possible introduction of noise by active components during integration, and for performing the required baseline subtraction. The diagnostic on the STOR-1M was used to calculate poloidal beta and average plasma kinetic pressure values. These were found to be $\beta_\theta \simeq 0.5$ and $\langle nT \rangle = 160 \text{ J/m}^3$, in good agreement with experimental results from Wolfe [77] for Ohmic discharges. $\beta_\theta > 1$ and $\langle nT \rangle = 200 \text{ J/m}^3$ were found for Ohmic discharges with turbulent heating, in fair agreement with Sarkissian [78].

4.2 Implementation of Coils on STOR-M

The method implemented on STOR-M is similar to the STOR-1M method. A single coil is used to measure the flux from plasma diamagnetism, while additional coils are used to compensate stray fields and vibrations. A vacuum baseline shot is used to further compensate the background fluxes. The following subsections outline the requirements and design of the coils implemented on STOR-M.

4.2.1 Requirements for STOR-M

The expected signal on the diamagnetic loop can be readily estimated from Eq. (2.24), and from shot data:

$$V_p = \frac{d}{dt} \Delta \Phi_p = \frac{\mu_0^2 (1 - \beta_\theta)}{8\pi} \frac{d}{dt} \left(\frac{I_p^2}{B_T} \right) \quad (4.3)$$

In the above, plasma current and toroidal magnetic field are time dependent, while poloidal beta is assumed a constant value ($\beta_\theta = 0.5$, based on prior Spitzer based

measurements). From the results of estimations for a typical shot (Fig. 4.1), the maximum expected signal is approximately 4 mV, while the expected signal during the plateau (steady state) region of the plasma discharge is near 0.5 mV in magnitude.

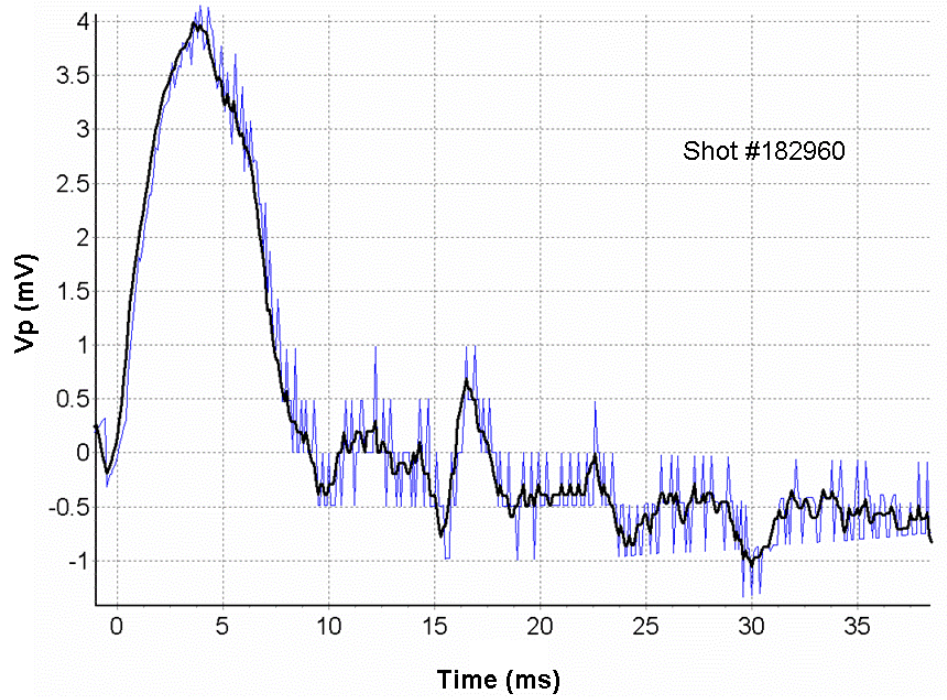


Figure 4.1: Expected induced diamagnetic loop voltage for typical shot. Thin line indicates raw calculations. Thick line is 5 point average of V_p . This calculated signal does not include the influence of noise.

Clearly, low noise, high fidelity processing is required.

4.2.2 Primary Compensation

The diamagnetic flux is quite small when compared to the total magnetic flux produced. The measured flux is further reduced by the loop radius r_c being larger than the plasma radius a . The required precision for the diamagnetic flux measurements can be estimated from:

$$\frac{\Delta\Phi_m}{\Phi_{\phi_e}} = \frac{a^2 B_{\theta}^2(a)}{r_c^2 2B_{\phi_e}^2} (1 - \beta_{\theta}) \quad (4.4)$$

where Φ_{ϕ_e} is the externally applied BT flux, a is the plasma minor radius, r_c is the radius of the diamagnetic coil, B_θ is the poloidal magnetic field, B_{ϕ_e} is the externally applied toroidal magnetic field, and β_θ is the poloidal beta quantity.

For STOR-M parameters ($a = 12.5$ cm, $I_p = 20$ kA, $B_{\phi_e} = 1$ T, $\beta_\theta = 0.5$) and an approximate loop radius of $r_c = 15$ cm, an estimate of $\simeq 2 \times 10^{-4}$ is acquired:

$$\frac{\Delta\Phi}{\Phi_{\phi_e}} = \left(\frac{12.5\text{cm}}{15\text{cm}}\right)^2 \frac{(1 - \beta_\theta)}{2(1\text{T})^2} \left(\frac{4\pi \times 10^{-7}\text{WbA}^{-1}\text{m}^{-1} \cdot 20 \times 10^3\text{A}}{2\pi \cdot 12.5 \times 10^{-2}\text{m}}\right)^2 \simeq 1.78 \times 10^{-4} \quad (4.5)$$

This indicates that measurements of flux must be better than 1 part in 10^5 to achieve even a 10% accuracy. Since the loop will sample all present fluxes, noise must be limited, and compensation for the undesired fields is required.

4.2.3 Vibrational Compensation

Vibration of the structure during a shot can impact the measurement of diamagnetic flux. As the coils vibrate, they move through a strong magnetic gradient and undesired signals are induced. For a single turn loop, the ratio of the mechanically generated signal Δe to the diamagnetic signal [79] is given by:

$$\frac{\Delta e}{\Delta\Phi} = 4q_b^2 \frac{R^2}{a^2} \frac{\Delta R}{R} \frac{1}{\beta_\theta - 1} \quad (4.6)$$

where ΔR is amplitude of mechanical vibration, R is the toroidal major radius, and a is the toroidal minor radius. Using typical values for STOR-M ($q_b = 3$, $R = 46$ cm, $a = 12.5$ cm, $\beta_\theta = 0.5$) and assuming vibration of 3 mm, Eq. (4.6) predicts a ratio of $\simeq 6:1$. This problem can be compensated for firstly by reducing vibration by mechanically isolating the coil from the structure, as well as electrically through the use of compensating coils. The effects of vibration are minimized by mechanically isolating the coil form from the vacuum chamber. However, since vibrations of even 1/10 of a millimeter are still nearly the order of the signal, electronic compensation may still be necessary. The auxiliary coils are used for this compensation. When the inner and outer coils of the system are balanced by a gain α , their signals will cancel out:

$$|\alpha A_{inner} B_{\phi_{inner}}| = |A_{outer} B_{\phi_{outer}}| \quad (4.7)$$

where A and B_ϕ are the effective area and toroidal magnetic field flux of the inner and outer coils. As vibrations cause motion in the coils, the balance is defeated and a signal proportional to the vibration is created.

4.2.4 Effect of Chamber Walls

Of primary consideration of the design is the location of the coils. The coils may be mounted either internally or externally on the vacuum chamber. For coils mounted externally, the bandwidth available from the signal is limited by eddy (Foucault) currents which appear in the chamber walls in response to changing magnetic fields. This skin effect imposes an upper frequency cutoff. Due to the restriction on bandwidth, the timescales available for study are also limited. The propagation constant of a wave through media is a complex number [80] given by

$$k_c = \omega\sqrt{\mu\epsilon_c} = \alpha + j\beta \quad (4.8)$$

where ω is the angular frequency of the wave, μ is the permeability of the material, and ϵ_c is the complex permittivity of the material given by

$$\epsilon_c = \epsilon \left(1 - j\frac{\sigma}{\omega\epsilon} \right) \quad (4.9)$$

which for conductivity $\sigma \gg \omega\epsilon_0$ can be written

$$\epsilon_c = -j\frac{\sigma}{\omega} \quad (4.10)$$

and the constant α and β are expressed as

$$\alpha = \sqrt{\frac{\omega\mu_0\sigma}{2}} = \frac{1}{\delta} \quad (4.11)$$

$$\beta = -\frac{1}{\delta} \quad (4.12)$$

where δ is the skin depth (defined as the distance traveled by a traveling plane wave through a material such that its amplitude is decreased by a factor of e^{-1}) [81, 82]. For good conductors, the skin depth can be defined as

$$\delta = \frac{1}{\sqrt{\pi f \mu \sigma}} \quad (4.13)$$

The solution of the wave equation can be written to represent a uniform wave propagating in the $+z$ direction.

$$E_x = E_0 e^{-\alpha z} e^{-j\beta z} \quad (4.14)$$

For STOR-M, there are two possible mounting locations. One is over the stainless steel bellows where the thickness is 0.5 mm. The other is over the stainless steel chamber walls where the thickness is 4 mm. The conductivity of the stainless steel is $\sigma = 1.45 \times 10^6 \text{ } \Omega^{-1}/\text{m}$. The attenuation due to the skin effect at these locations is plotted in Fig. 4.2

Mounting the coil internally provides significantly higher bandwidth, but at the cost of a valuable diagnostic port. The limiting time scale imposed by the chamber walls [83] is given as:

$$T_1 \simeq 5\sigma\mu_0 \left(\frac{t_w}{\pi}\right)^2 \quad (4.15)$$

where σ and t_w are the conductivity and thickness of the chamber wall, respectively. For the STOR-M ($t_w = 4 \text{ mm}$, $\sigma = 1.45 \times 10^6 \text{ } \Omega^{-1}/\text{m}$), a time scale of $\simeq 15 \text{ } \mu\text{s}$ is estimated. Taking the cutoff frequency to be $f_c = 1/2T_1$, a limiting frequency of $\simeq 30 \text{ kHz}$ is found. In the work of Rothman [84] the factor of 5 is removed from equation (4.15) and the cutoff frequency is increased accordingly to $\simeq 170 \text{ kHz}$. The lower estimate is chosen for consideration. There is also the option of mounting the coils around the bellows section of the chamber where the thickness is $\simeq 0.5 \text{ mm}$. This section affords a cutoff frequency on the order of 2 MHz. Since mounting interior to the chamber walls would likely require some kind of protection for the coils (ie, stainless steel tubing), and such protection of any appreciable thickness would

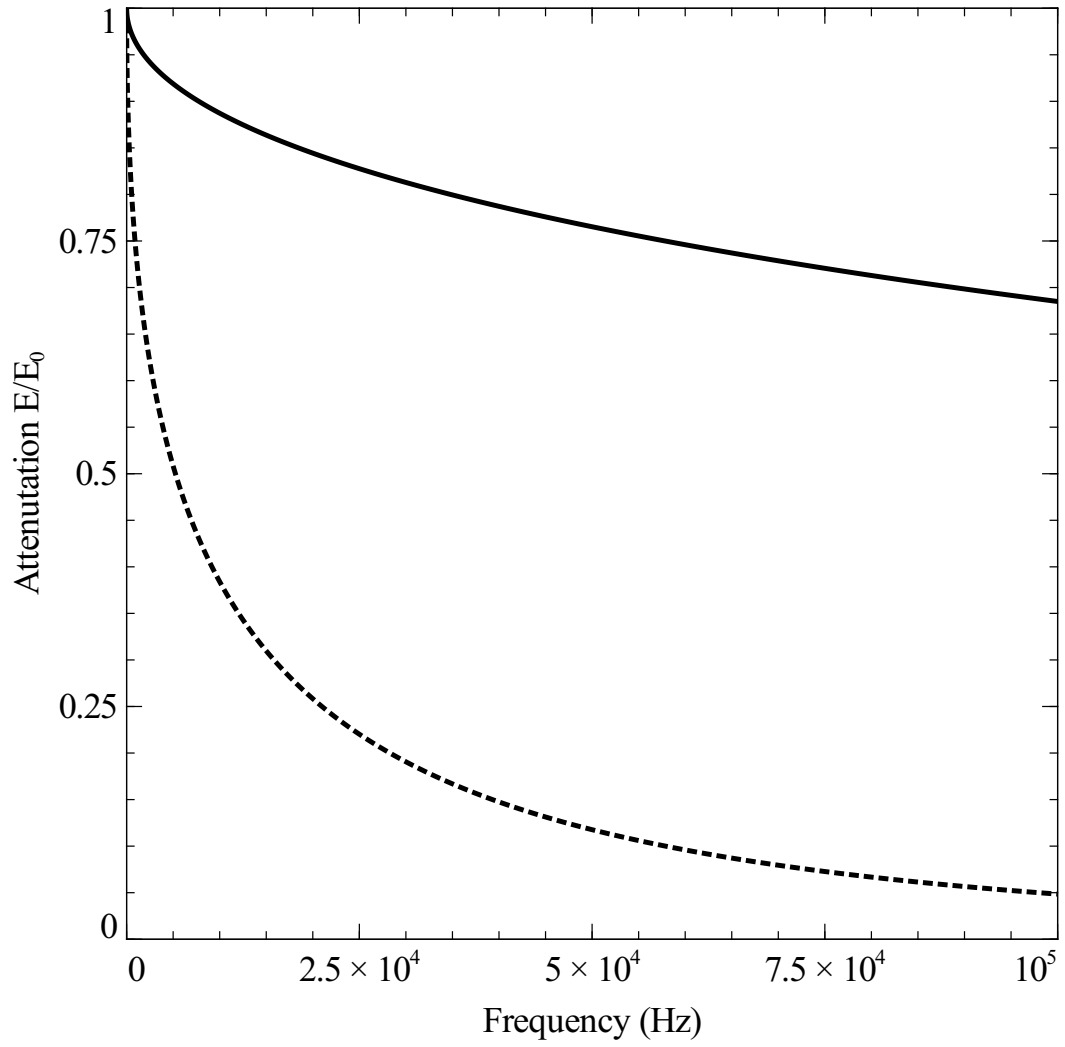


Figure 4.2: The attenuation of the signal due to the skin effect at the bellows (solid line) and the chamber walls (dotted line)

be competitive with the bellows, the bellows offer a great alternative to interior mounting even for high bandwidth requirements.

The skin time at the thinner bellows section (0.5 mm stainless steel) is $\tau_s \approx 1.5 \mu\text{s}$. The skin time at the thicker stainless steel chamber wall (5 mm) is $\tau_s \approx 15 \mu\text{s}$. The overall skin time is expected to be between these two values, and will be much smaller than the expected characteristic time of plasma equilibrium evolution, which is on the order of a millisecond. The filtering effect of the vacuum chamber does not prevent this measurement from being performed externally. The attenuation of the signal due to the chamber (bellows section) has been estimated by skin effect calculation (modeling the flexible bellows as a cylinder) to be approximately 0.8 (significantly better than the chamber walls where the attenuation factor is approximately 0.3), meaning the exterior mounting is acceptable in terms of signal strength. The skin effect will also introduce a phase delay, however this is not important for diamagnetic measurements.

4.2.5 Baseline Compensation Methodology

For external mounting of the diamagnetic coil system, magnetic flux introduced by poloidal currents induced in the tokamak chamber walls can not be properly compensated for using this set of coils because this flux is located inside the chamber only (neglecting the effects of flux leakage). In the case of constant toroidal magnetic field during the plasma discharge, this induced current is absent, and does not introduce magnetic flux. In the STOR-M tokamak, the toroidal magnetic field decreases by about 20% over the discharge and introduces a significant image current. In order to take this effect into account, a simple experimental technique with non-plasma shot data for additional compensation is adopted. Typically, more complicated systems relying on software [66, 70] are used for fully compensating externally mounted coils. It is expected that for a machine with as large a drift of TF as STOR-M has, the so called error flux or residual flux will be much larger than these machines previously reporting external diamagnetic measurement methods. In STOR-M, the problem of residual flux due to image currents in the measurements is handled by use of

a blank (non-plasma) shot. The fluxes sampled by the enclosing loop ϕ_1 , and the non-enclosing loop ϕ_2 , during a blank (non-plasma producing shot) are

$$\phi_1 = \phi_{BT1} + \phi_{err} \quad (4.16)$$

$$\phi_2 = \phi_{BT2} \quad (4.17)$$

where ϕ_{BT} is the flux due to the background toroidal field picked up by each coil, ϕ_{err} is residual flux picked up by the enclosing coil, but not by the non-enclosing coil. This residual flux is likely due to image currents in the chambers walls arising due to the presence of the toroidal field coil current. A gain constant, α is introduced to set $\phi_{BT1} = \alpha\phi_{BT2}$, and subtraction of these fluxes yields

$$(\phi_1^b - \alpha\phi_2^b) = \phi_{err}^b \quad (4.18)$$

where the subscript b indicates the shots were taken without plasma. The gain constant, α is chosen such that the subtraction of the two coils produces a minimum value. The gain constant allows the BT flux sampled by the second coil (non-enclosing loop) to eliminate both TF and the proportional image current term from the first coil (single loop). Performing a blank shot allows collection of the residual flux due to residual image current term alone which can then be eliminated from the plasma bearing shots. The fluxes sampled by the enclosing loop ϕ_1 , and the non-enclosing loop ϕ_2 , during a plasma producing shot are

$$\phi_1 = \phi_{BT1} + \phi_{err}^p + \delta\Phi + \delta\phi_{ic,\Delta\Phi} \quad (4.19)$$

$$\phi_2 = \phi_{BT2} \quad (4.20)$$

where again, ϕ_{BT} is the flux due to the toroidal field coils, ϕ_{err}^p is the residual flux appearing due to residual image currents not proportional to the TF coil current, $\delta\Phi$ is the flux from plasma diamagnetism and paramagnetism, and $\delta\phi_{ic,\Delta\Phi}$ is the additional flux (separate from ϕ_{err}^p) due to the additional image currents on the chamber

induced by the combined paramagnetic and diamagnetic plasma current. Subtraction of these fluxes yields

$$(\phi_1^p - \alpha\phi_2^p) = \phi_{err}^p + \delta\Phi + \delta\phi_{ic,\Delta\Phi} \quad (4.21)$$

The blank shot data (Eq. 4.18) is subtracted from the plasma shot data (Eq. 4.21), yielding

$$(\phi_1^b - \alpha\phi_2^b) - (\phi_1^p - \alpha\phi_2^p) = \delta\Phi + (\phi_{err}^p - \phi_{err}^b) + \delta\phi_{ic,\Delta\Phi} \quad (4.22)$$

The presented method requires that the residual image currents present in the blank and plasma shots are identical, and the stray flux due to toroidal currents (such as plasma current, Ohmic heating coil current, and vertical field coil current), does not significantly contribute to these residual image currents. (This assumption is expected to be reasonable in stable plasma discharges, if the current in the toroidal field coils dominates the residual signal. This condition is examined in the results section. It is then necessary to examine the condition

$$\phi_{err}^p = \phi_{err}^b \quad (4.23)$$

which allows for the elimination of the residual flux by the method of baseline subtraction used in this paper. If the image current in the chamber walls is considered

$$R_c I_c = -L_c \dot{I}_c - M_{c,BT} \dot{I}_{BT} - \Delta \dot{\Phi} \quad (4.24)$$

where R_c is the poloidal resistance of the chamber walls, L_c is the wall inductance, and $M_{c,BT}$ is the mutual inductance between the chamber walls and the toroidal field coils. The use of a Laplace transform allows the image current term to be found

$$I_c = -\frac{M_{c,BT}}{R_c + sL_c} s I_{BT} - \frac{1}{R_c + sL_c} s \Delta \Phi \quad (4.25)$$

The enclosing loop measures the flux induced by this eddy current as $M_{1,c}I_c$. The two terms in the above equation can then be used to find the terms in Eq. (4.22)

$$(\phi_{err}^p - \phi_{err}^b) = -\frac{sM_{c,BT}}{1 + s\tau_c} (I_{BT}^p - I_{BT}^b) \quad (4.26)$$

$$\delta\phi_{ic,\Delta\Phi} = -\frac{sM_{c,BT}}{1 + s\tau_c} \Delta\Phi \quad (4.27)$$

where $\tau_c = L_c/R_c$ is the time constant of the eddy currents in the chamber walls. Based upon the dimensions of the stainless steel vacuum chamber, the chamber resistance has been found to be $61 \mu\Omega$, and the chamber inductance has been found to be $0.038\mu\text{H}$. This results in $L/R = \tau_c = 0.58 \text{ ms}$. Since the variation of the diamagnetic flux is slower than τ_c , $\delta\phi_{ic,\Delta\Phi}$ can be neglected. Eq. (4.26) predicts that the plasma and blank residuals are identical in the case where τ_c is sufficiently less than the characteristic time variation in the toroidal field currents, I_{BT} . In STOR-M, this time is approximately $\tau_{BT} = 250 \text{ ms}$ based on the approximately 20% decay in toroidal field observed over 50 ms. The limiting value of τ_c is approximately 125 ms, and therefore this term in equation 4 can be neglected. This limitation is examined by requiring the contribution of Eq. (4.27) to be no greater than 10% of $\Delta\Phi$, and is found by

$$(\phi_{err}^p - \phi_{err}^b) = -\frac{\tau_c}{\tau_{BT}} \times 0.0002 \times 100 \times \Delta\Phi < 0.1 \times \Delta\Phi \quad (4.28)$$

where the difference $(I_{BT}^p - I_{BT}^b)$ has been estimated to be about $0.002I_{BT}$ based on measurements made at the toroidal feed line by a Rogowski coil, and the mutual inductance between the chamber and the toroidal field current has been assumed equal to that of the diamagnetic coil and the toroidal field current, $M_{c,BT}I_{BT} \simeq M_{1,BT}I_{BT}$, which in general is about 100 times larger than the diamagnetic current. Examination of equation 6 shows that the $(\phi_{err}^p - \phi_{err}^b)$ term is expected to contribute approximately .04% error to the measurement of $\Delta\Phi$, and can therefore be neglected. Eq. (4.22) then becomes

$$(\phi_1^b - \alpha\phi_2^b) - (\phi_1^p - \alpha\phi_2^p) = \Delta\Phi \quad (4.29)$$

4.2.6 Coil Design

A polyoxymethylene plastic (trade name Delrin from DuPont) form is used to mount the coils. This material was chosen for strength, and for low conductivity. The compensation and auxiliary coils are made from 8 turns of 28 AWG magnet wire, while the primary coil is a single loop of the same type of wire. Special attention is required to reduce the influence of electrical noise on the signal [85–89]. Twisted pair cable is used to reduce noise pickup by the coil leads. All twisted pairs exiting the coil form are enclosed in a specially constructed shielded cable, which leads to a DA-15 female connector. The cable was purposely routed so as to not cross through the vertical plane of the machine, helping to minimize electromagnetic noise pick up. A male DA-15 connector mounted on a shielded distribution box near the tokamak allows for signal acquisition through male BNC connectors. The shielding efforts resulted in a sufficiently clean signal delivered to the data acquisition system. Signal measurements were made by connecting the coils through the distribution box directly to a National Instruments PCI-6133 data collection card [90] which provides sufficient resolution (14 bit over a 1 V range yielding 0.012% accuracy), and were processed on a computer. Plasma current and externally applied toroidal field are recorded by a lower resolution LeCroy unit [91]. Mechanical isolation of the diamagnetic coil assembly from the vacuum chamber was achieved by mounting the directly to the massive phenolic yoke structures support for the TF coils, where the level of vibration is estimated to be about 0.1 mm. This reduces the vibration induced error signal to approximately 6.5% of the diamagnetic signal (based on equation 4.6). These signals are then electrically compensated for using a set of auxiliary coils arranged in opposition such that their signals cancel in the absence of vibrations, greatly reducing the contribution of vibration errors. This is a benefit of mounting the coils external to the chamber compared with internally mounted

coils, which present significantly larger vibration errors. The mounted assembly is pictured in Fig. 4.3. Due to the exterior mounting of the coils, two major concerns arise. The first is that the signal will be attenuated and potentially filtered (cut off) due to the effects of eddy currents in the stainless steel chamber. The second is that image currents resulting in the chamber walls are not sampled by the non-enclosing compensation coil. Since the non-enclosing coil does not directly link the flux due to image currents, it must be compensated for separately. There is some minor flux leakage, but in general the residual signal from the image currents is not compensated by this coil configuration.

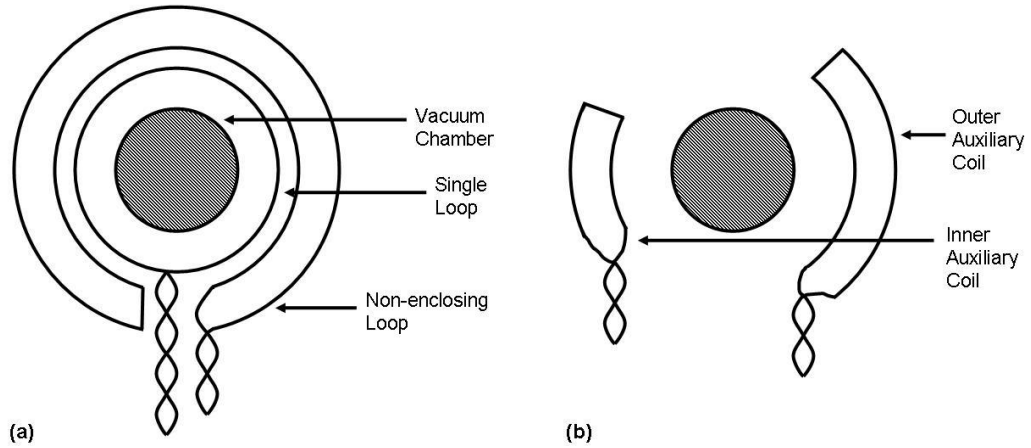


Figure 4.3: (a) The primary (single loop) coil and the compensating (non-enclosing) coil located outside the vacuum chamber. (b) The set of auxiliary compensation coils. Although these coils are shown separately for clarity, they are installed coplanar in the same form.

The four coils produce the following voltages: The voltage arising in the single loop coil, V_{Dm} , the voltage arising in the compensation coil, V_c , the voltage arising in the inner auxiliary coil, $V_{aux-inner}$, and the voltage arising in the outer auxiliary coil, $V_{aux-outer}$. The compensated signal is acquired from

$$V_{meas} = V_{Dm} - k_1 V_c - k_2 (V_{aux-inner} - k_3 V_{aux-outer}) \quad (4.30)$$

where k_1 , k_2 , k_3 are gain constants satisfying the condition that V_{meas} is a minimum

in the absence of plasma. The method of determining these gain constants is as follows:

1. k_1 is chosen such that result of $V_{Dm} - k_1 V_c$ is at a minimum for blank shot data.
2. k_2 is chosen such that the result of $V_{aux-inner} - k_2 V_{aux-outer}$ is at a minimum for blank shot data.
3. k_3 is then chosen such that V_{meas} is at a minimum for blank shot data.

The measured voltage during a plasma producing shot is then compensated by the residual voltage (minimum measurement of V_{meas}) measured during a blank shot. When integrated numerically, the vacuum compensated measured voltage provides $\Delta\Phi$, the change in plasma flux due to paramagnetism and diamagnetism.

4.2.7 Coil properties

The resistance, capacitance, and inductance of the diamagnetic coils was measured with an LCR meter at frequencies of 100 Hz, 120 Hz, 1 kHz, and 10 kHz. The results are shown in table 4.1.

4.3 Error Budget

The complete error budget for the project is given in tables 4.2 and 4.3. Error due to the reproducibility of the blank shots has been found to be 3% by direct comparison of multiple blank shots. Errors due to potential misalignment of the coil in the poloidal plane were found to be negligible by experiment. Overall error in the measured value of poloidal beta during stable plasma operation is estimated at 5.6%, based on quadrature addition of the errors introduced by hardware limitations of the data acquisition system, and the statistical error of the blank shots due to the TF image currents and non-constant plasma current.

| Coil | 100 Hz | 120 Hz | 1 kHz | 10 kHz |
|------------------------------|--------|--------|-------|--------|
| Inductance [μH] | | | | |
| Dm | 1 | 7 | 9.6 | 1.4 |
| P | 92 | 230 | 104 | 90 |
| Ai | 27 | 122 | 4.5 | 27.7 |
| Ao | 23 | 13 | 6.3 | 17.9 |
| Capacitance [nF] | | | | |
| Dm | 10,000 | 3,000 | N/A | 455 |
| P | 1,400 | 540 | 325 | 280 |
| Ai | N/A | 1,680 | 740 | 655 |
| Ao | 4,500 | N/A | 940 | 760 |
| Resistance [Ω] | | | | |
| Dm | 2.4 | 2.4 | 2.3 | 2.2 |
| P | 17.5 | 17.5 | 17.5 | 19.0 |
| Ai | 6.5 | 6.5 | 6.5 | 6.9 |
| Ao | 4.9 | 4.9 | 4.9 | 5.1 |

Table 4.1: Inductance, Capacitance, and Resistance measurements of the Diamagnetic Coils. Properties are shown for the single loop coil (Dm), the primary compensation coil (P), the inner auxiliary coil (Ai) and the outer auxiliary coil (Ao).

| Source | Error |
|--|-------|
| 3 mm magnitude vibrations (chamber mounting) | 195% |
| Assumption of constant BT | 18.5% |
| Assumption of constant plasma current | 15.0% |
| NI 6133 14 bit resolution of 5 mV signal (raw input, 10 V range) | 12.0% |
| 0.1 mm magnitude vibrations (mechanical isolation) | 6.50% |

Table 4.2: Eliminated Errors for Diamagnetic Diagnostics

| Source | Error |
|--|--------------|
| Background electrical noise (non-tokamak) (raw input) | 3.60% |
| Statistical error of residual signal | 3.0% |
| NI 6133 14 bit resolution of 5 mV signal (raw input, 1 V range) | 2.4% |
| noise generated by CT | 2.0% |
| NI 6133 noise (1.25V range, 5 mV input) (raw input) | 1.38% |
| 12 bit resolution of 0.2 V Ip input signal | 1.25% |
| Variations in charging voltages | 1.00% |
| LM6181 line driver estimate noise (per channel) | 0.050% |
| Lecroy 12 bit resolution limit (5V signals) | 0.050% |
| Image currents induced by diamagnetic / paramagnetic plasma currents | 0.040% |
| NI 6133 14 bit resolution limit (10 V signals) | 0.012% |
| Background electrical noise (non-tokamak) (10V gain signals) | 0.004% |
| double class 15 digit resolution (delphi software) | < 0.001% |
| AD620 preamp estimated noise (per channel) | < 0.001% |
| NI 6133 noise (10 V range, 10 V signal) | < 0.001% |
| NI 6133 noise (1.25 V range, 1.25 V input) | < 0.001% |

Table 4.3: Remaining Error Budget for Diamagnetic Diagnostics

CHAPTER 5

EXPERIMENTAL RESULTS

5.1 Experimental Outline

Two primary experiments are presented in this section. In the first experiment, the performance of the diamagnetic coils is examined under normal ohmic discharge conditions. The residual vacuum baseline signal is examined and the diamagnetic measurement of poloidal beta is compared to poloidal beta calculated by measurements of Spitzer temperature. Reasonable agreement between the two methods is found. The second experiment tests the operation of the diamagnetic system with the Compact Toroid Injector. Neutral gas injection from CT, CT Injection, and normal ohmic discharges are compared. The change in plasma bulk thermal energy is diamagnetically measured for CT injection. The density evolution and Soft X-Ray emission evolution between CT and neutral gas injection is compared. Diamagnetic measurements of poloidal beta and SXR behavior are examined. It was found that the electromagnetic noise from the CT did not significantly affect the diamagnetic measurement. A sharp increase in poloidal beta due to CT injection was observed.

5.2 Ohmic Discharge Experiments

A series of normal ohmic discharges (Fig. 5.1) was conducted and data was collected from the coils. The measured signal from the diamagnetic coils was compensated with signals recorded during the execution of a blank shot. In this shot, steady-fill and gas puffing was disabled and the tokamak coils (toroidal field, ohmic heating, feedback, etc...) were energized while the chamber was held at vacuum. The mea-

sured signal from the blank was then subtracted from the signal measured during normal operation. Figure 5.2a shows the magnitudes of the raw measurements of $\Delta\Phi$ taken from blank and from plasma shots, as well as the final compensated data. Fig. 5.2b shows that the primary contribution to the blank shot is the toroidal field coils. Contributions from the automatic feedback system (FB) and the ohmic heating coils (OH) are quite small by comparison. This is especially important as the toroidal field charging system exhibits strong repeatability of better than 3% based on experimental measurements. The actual toroidal field produced shows excellent repeatability shot to shot. Variations in the toroidal field find their way in the measurement through induced image currents (the blank shot signal shown in Figure 5.2). The FB and OH system signals can strongly depend on plasma conditions, which could potentially be a large source of error in the blank shot compensation. Fortunately, FB and OH fluxes do not play major role in the acquired signal. Fig. 5.2c shows the relative contributions of fluxes produced by the FB and OH systems compared to the compensated flux signal. FB and OH signals were produced by subtraction of the BT, BT+ FB, and the BT+FB+OH signals in Fig. 5.2b. The FB signal is a maximum contribution, as the FB system saturates in the absence of plasma. The OH contribution may be at a minimum, since there is no plasma for the OH coils to link to. The results of Fig 5.2 show that FB and OH fluxes are not significant compared to either the contribution of BT to the residual, or to the diamagnetic measurement.

Flux measurements and poloidal beta calculations are presented in Fig. 5.3. Figure 5.3 shows the expected peak in $\Delta\Phi$ near 10 ms corresponding to the peak in plasma current. Poloidal beta is calculated from the measured flux to be near 0.5 (paramagnetic) throughout the flat top portion of the discharge. Bulk thermal energy and confinement time were calculated from the poloidal beta quantity. In the time following 20 ms, the decaying plasma current and plasma density lead to unstable readings from the coil system. It is a primary shortcoming of external mounted diamagnetic coils that poor plasma behavior can produce undesired, uncompensated signals in the coils through image currents produced in the chamber walls. Likewise,

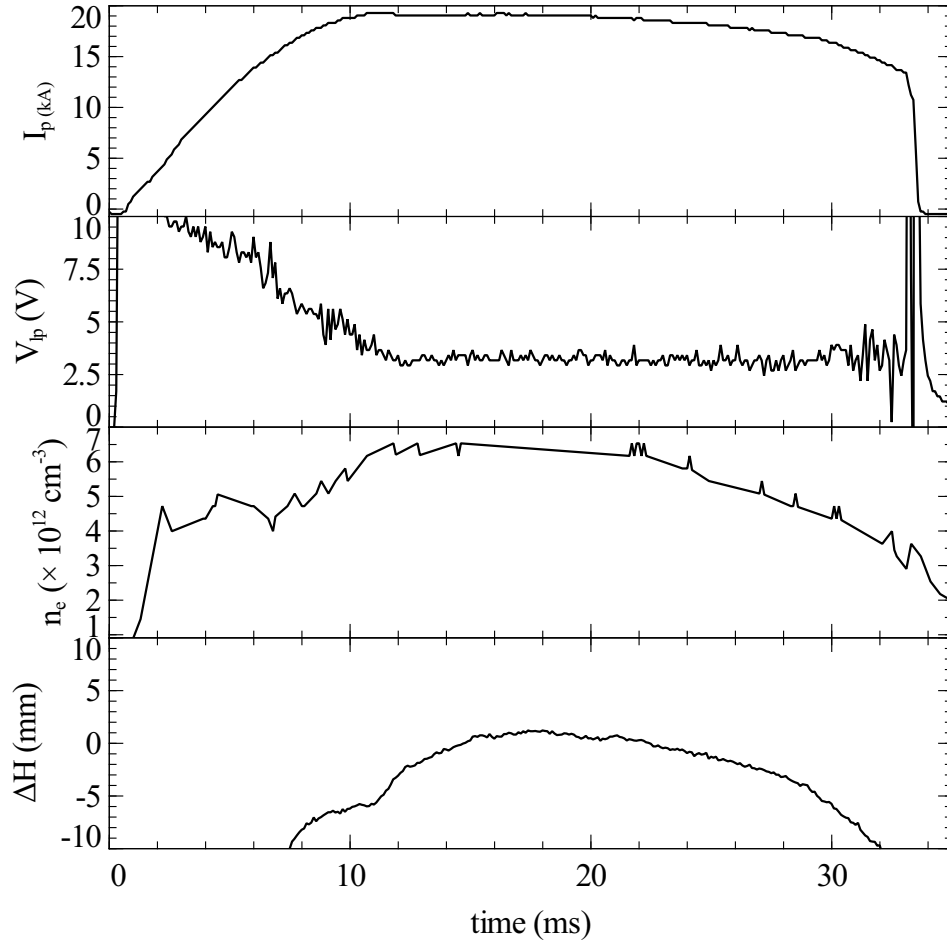


Figure 5.1: Plasma current, loop voltage, average electron density, and plasma position for a typical normal ohmic discharge. Shot 204760.

the time prior to 10 ms when the plasma is undergoing breakdown and subsequent current ramp up is also unreliable since the poloidal beta term is proportional to $\Delta\Phi/I_p^2$. However, this section is shown to help illustrate that the peak in measured flux is where it is expected to be.

The measured values of poloidal beta are compared to values obtained from Spitzer resistivity calculations in Figure 5.4. Reasonable agreement between the two independent methods is shown. The Spitzer resistivity calculations suffer from the assumption that the effective ion charge of the plasma Z_{eff} is constant at a value of 1.5 in STOR-M. It has been observed that large, rapid variations in plasma position

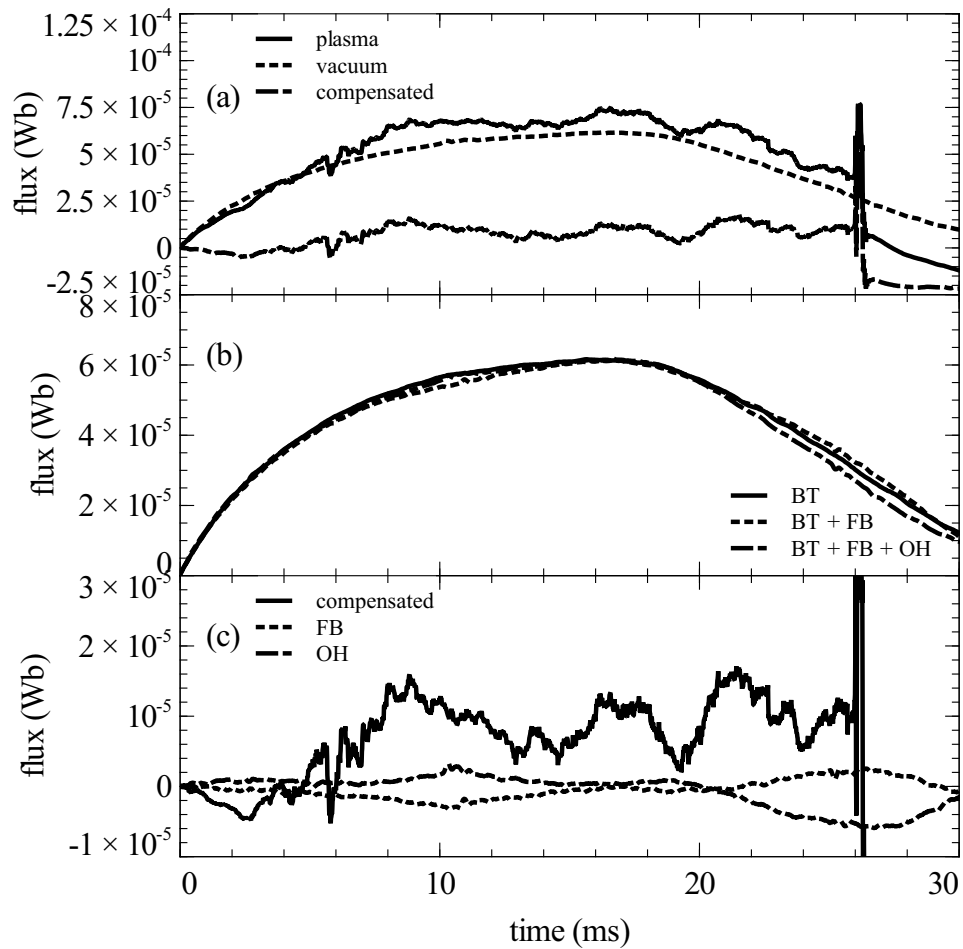


Figure 5.2: (a) Plasma, vacuum, and compensated flux signals. (b) Contribution of the toroidal field coils (BT), position feedback system (FB), and ohmic heating coils (OH) to the blank shot baseline. (c) Relative sizes of the feedback and OH contributions to the final compensated shot. Shot 204760.

can severely affect the accuracy of this diagnostic. Several shots with poor feedback control were examined and oscillating behaviors in the plasma position were observed to appear in the measured flux signal. In the case of unstable (large position shift) plasmas, the diagnostic is unreliable. Further, when position control is so poor that the plasma touches the chamber walls, the plasma is no longer in equilibrium and the assumptions behind the derivation of the poloidal beta calculations fail to hold. Error due to the reproducibility of the blank shots has been found to be 3% by direct comparison of multiple blank shots. Errors due to misalignment of the coil in the

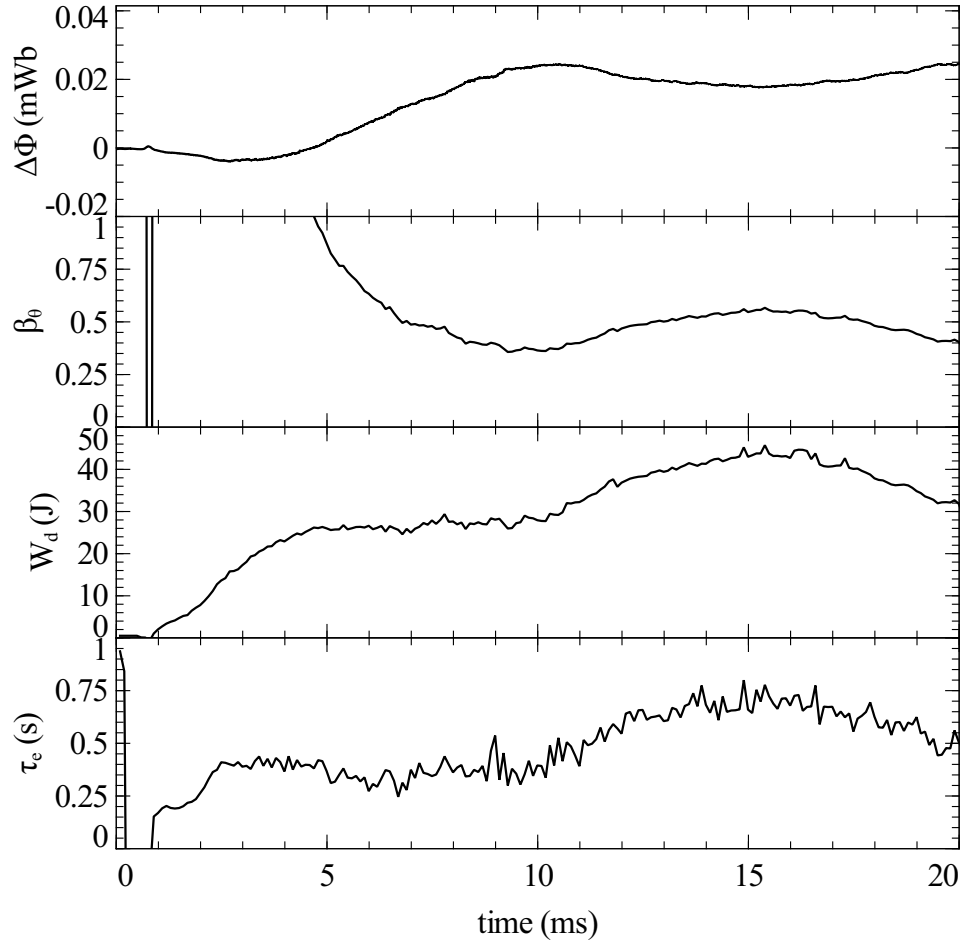


Figure 5.3: Measured toroidal flux change, poloidal beta, bulk thermal energy, and energy confinement time. Shot 204760.

poloidal plane were found to be negligible by experiment.

5.3 Compact Toroid Injection Experiments

Figure 5.5 shows the plasma current, loop voltage, and H_α emissions for the CT Injection discharge 209987. The dashed line in Fig. 5.5c shows the level of H_α emission for the normal ohmic discharge. It is clear that CT injection caused a reduction in H_α emission.

Figure 5.6 shows a comparison of line averaged electron density, Soft X-Ray emission, and poloidal beta between shots with CT injection, neutral gas puffing from the

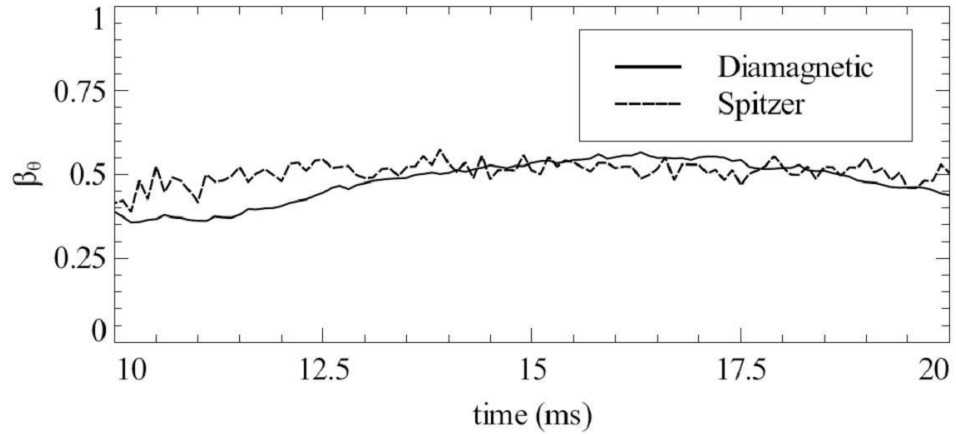


Figure 5.4: Comparison of diamagnetically measured and Spitzer based calculations of poloidal beta. Shot 204760.

USCTI, and a normal ohmic discharge. In Fig. 5.6a, density can be seen to increase due to CT injection. Density increase in the case of neutral gas from the USCTI is seen to be delayed compared to the CT injection scenario. This is expected, as the neutral gas must diffuse down the drift tube, as opposed to the CT, which is actively accelerated. Both the CT injection and neutral gas discharges eventually arrive at nearly the same final density of $11 \times 10^{12} \text{ cm}^{-3}$ at 24 ms. However, the CT injection discharge shows a distinct initial jump in density following injection at 17 ms, similar to results reported from TdeV [92]. The dashed line in Fig. 5.6a indicates the density measured for a normal ohmic discharge. Soft X-Ray data (Fig. 5.6b) for the three scenarios shows that there is a strong increase in SXR emissions immediately following CT Injection. There is a smaller, delayed increase associated with the neutral gas scenario. The profiles of poloidal beta and SFX show very strong agreement. It is clear in both the case of neutral gas injection and CT injection that the diamagnetic measurements are responding to changes in the plasma $\langle nT \rangle$, as SXR emissions contain both temperature and density dependences. Ohmic discharge data shows SXR emissions steadily decreasing throughout the discharge. Poloidal beta measured by a diamagnetic loop is shown for the three discharge scenarios in Fig 5.6c. The CT Injection discharge shows a clear increase in poloidal beta following

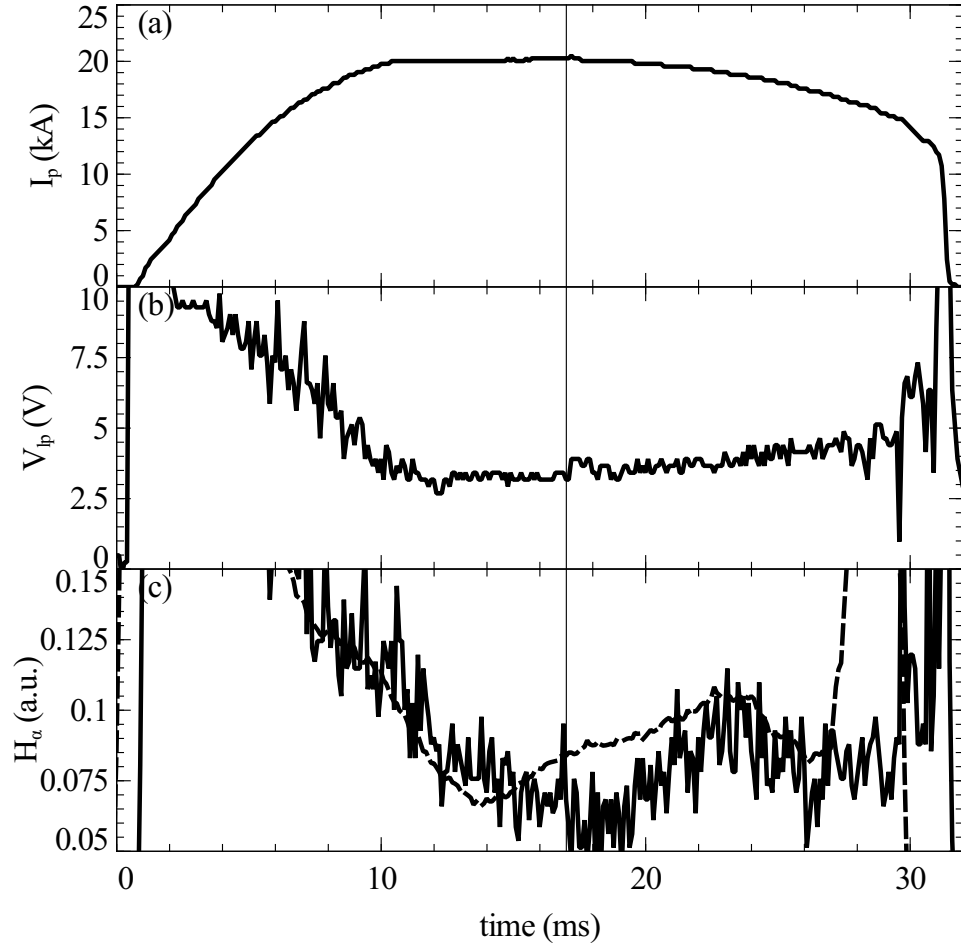


Figure 5.5: (a) Plasma current. (b) Loop Voltage. (c) H_{α} emission for CT Injection discharge 209987. The dashed line shows a normal ohmic discharge, and the vertical line shows the time of CT injection.

the injection. The neutral gas discharge shows poloidal beta decreasing until 20 ms, where it levels out. This corresponds to both the delayed increase in density, and the increasing SXR emissions that appear at the same time. The observed decrease in poloidal beta in all three discharges may be a systematic error of the measurement. A statistical survey of diamagnetic measurements reveals that the measurements typically show a decreasing drift in poloidal beta which appears following about 20 ms of discharge time. The influence of the toroidal field current on the image currents and the measurement was discussed earlier. It is expected that the drift appears due to the influence of plasma current on the chamber wall image currents.

The energy deposited by the CT was analyzed by use of the diamagnetic loop. Fig. 4 shows a 5.6 J increase in the plasma bulk kinetic energy following CT injection. Considering a CT life of 0.5 ms (based on poloidal beta rise time in Fig 2c) yields an average CT power of 11.2 kW. The measured power is in reasonable agreement with the previously reported estimate of 13 kW [28].

5.4 Summary of Experimental Results

5.4.1 Ohmic Discharge Experiments

Diamagnetic measurements using compensated coils mounted externally to the vacuum chamber with additional compensation from blank shots were performed on the STOR-M tokamak. The presented method provides reliable poloidal beta measurements during stable discharges with an error of 5.6%, with the major contribution being 3% from image currents which vary due to slight TF irreproducibility. The diamagnetically measured poloidal beta was compared to poloidal beta from Spitzer resistivity and was seen to agree well. It is likely that the assumption of constant $Z_\sigma = 1.5$, and the assumption that $T_i = \frac{1}{3}T_e$ in the Spitzer measurements contribute to the slight discrepancy.

5.4.2 Compact Toroid Injection Experiments

The bulk plasma thermal energy change due to Compact Toroid Injection was measured using the diamagnetic coils. An increase of 5.6 J was observed following the injection of the CT. The differences in measured poloidal beta for the cases of CT injection, neutral gas injection from the CT gas valves, and normal ohmic operation were examined and compared to SXR measurements. CT injection was seen to immediately increase poloidal beta, density, and SXR emissions. In the case of neutral gas puffing, a delayed and much less dramatic increase is observed. Strong agreement between the increase of poloidal beta and the increase of SXR emissions is observed. A drift appears in the poloidal beta measurements later in the measurement (about

20 ms in). It is expected that this drift is due to image currents, and requires further compensation for increased measurement precision.

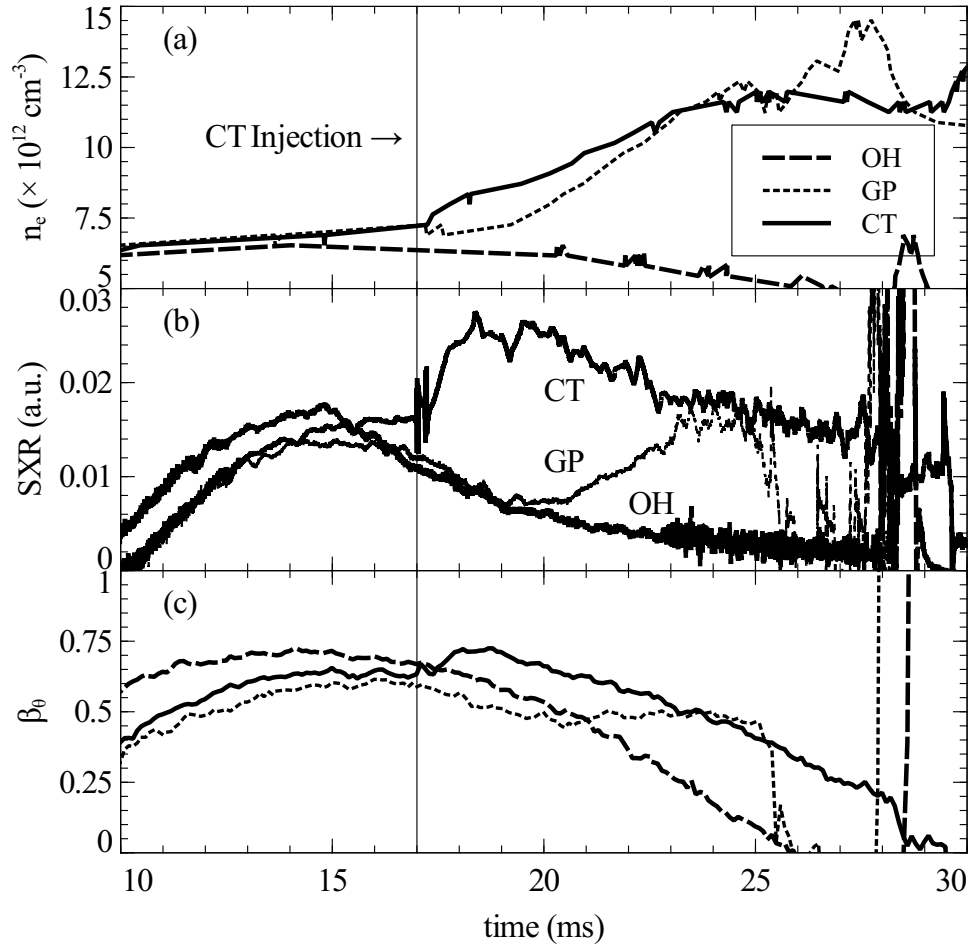


Figure 5.6: (a) Line averaged electron density. (b) Soft X-Ray emission. (c) Diamagnetically measured poloidal beta. Normal Ohmic (dashed line), Neutral Gas puffing from CT (dotted line), and CT Injection (solid line). The solid vertical line at 17 ms indicates the time of CT injection. Ohmic discharge 210021. Neutral Gas puffing from CT discharge 209985. CT Injection discharge 209987.

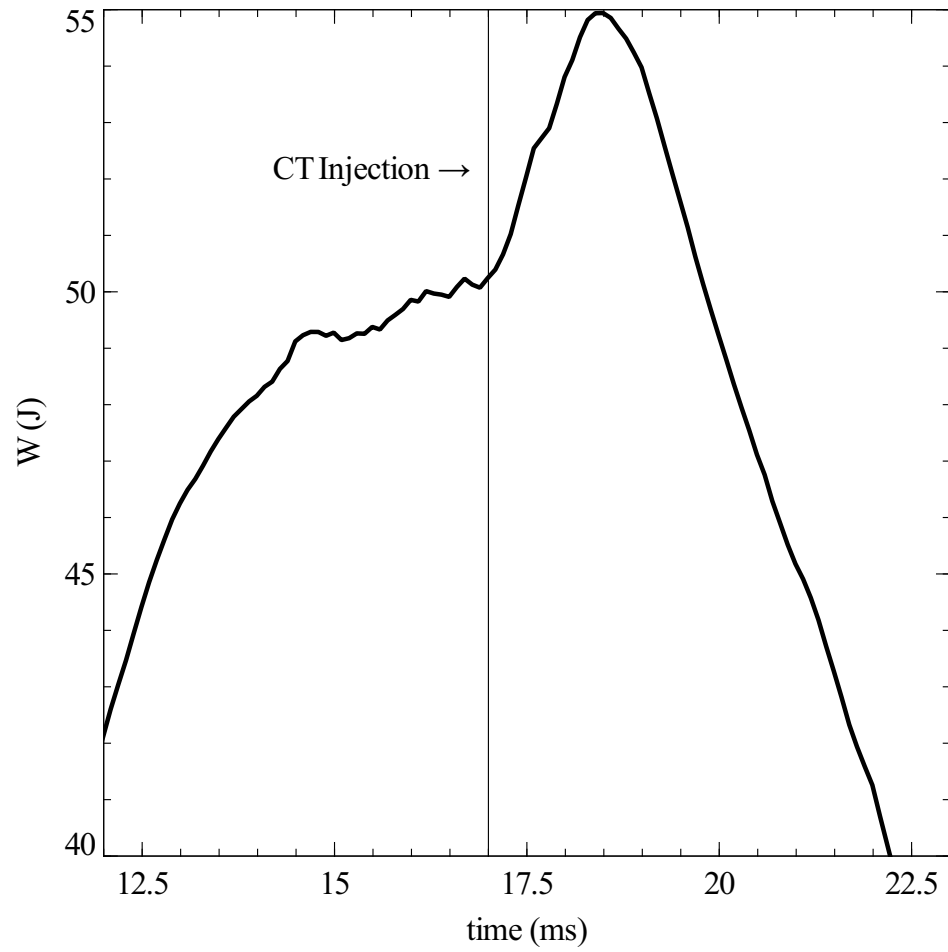


Figure 5.7: Diamagnetic measurement of the plasma bulk kinetic energy for CT Injection shot 209987.

CHAPTER 6

CONCLUSION AND FUTURE WORK

6.1 Conclusion

An external diamagnetic coil system was designed, constructed, and tested on the STOR-M tokamak. It was found that additional compensation from blank shots was necessary to acquire the diamagnetic signal. The blank shots compensate for a strong residual signal that is expected to be related to the toroidal field system based on experimental observations. It is likely that the residual is the result of image currents forming in the chamber walls that are not directly proportional to the toroidal field current. The coil system employed was tested against Spitzer temperature measurements, and reasonable agreement was found between the poloidal beta values calculated by both methods. A poloidal beta of 0.5 was found for normal ohmic discharges in STOR-M. The error in the poloidal beta measurement was estimated to be 5.6 %, with the primary contribution being a 3% statistical error from the baseline shots. The diamagnetic coils were used to examine the change in plasma bulk thermal energy during Compact Toroid Injection. The experiment showed that the noise produced by the CT is not significant to the diamagnetic measurement. CT injection was seen to increase the plasma bulk thermal energy by 5.6 J. The behavior of the diamagnetically measured poloidal beta was seen to agree with measurements of Soft X-Ray emissions. It was observed that the diamagnetic coil system did not perform well during shots with significant variation in plasma position. A signal proportional to the changes in plasma position becomes evident in the diamagnetic signal in the case of strongly oscillating plasma position. Similarly, strongly decreasing plasma currents lead to drifts in the diamagnetic signal, likely

due to increased magnitudes of image currents in the chamber walls.

6.2 Future Work

The inclusion of the diamagnetic coils in studies of plasma confinement will provide useful information about the behavior of the plasma bulk, which combined with diagnostics measuring the behavior in the SOL will provide more detailed analysis of transitions in plasma confinement. The Spitzer measurement is plagued with assumptions. The ratio of ion and electron temperatures is assumed, the value of Z_{eff} is assumed (and assumed to be constant), and the plasma inductance is assumed. Direct measurement of Z_{eff} using spectroscopy would help in improving the accuracy of this measurement. With an improved Spitzer measurement, the Spitzer and diamagnetic measurements can be used together to examine the assumptions of plasma inductance and the ion/electron temperature ratio.

6.2.1 Compensation of Chamber Image Currents

It may be possible to compensate for the image currents in the diamagnetic measurement. The primary contribution to the image currents is the toroidal field. Circuit modeling of the coils and chamber could allow for calculation of the image currents induced in the chamber walls during a discharge by direct measurement of the toroidal field current. If the image currents are known, they can be eliminated from the diamagnetic measurement.

The plasma also contributes to the image currents. It is expected that the reason for the signal drift appearing late in the diamagnetic measurement is the contribution of image currents induced by the plasma current. As the plasma current changes, the poloidal component of the plasma current also changes (see Chapter 1). Since the poloidal component varies, image currents can be severe. Further, the plasma position can affect the induced image currents by shifting the peaked plasma current profile into the high or low field side, altering the poloidal component of the plasma current.

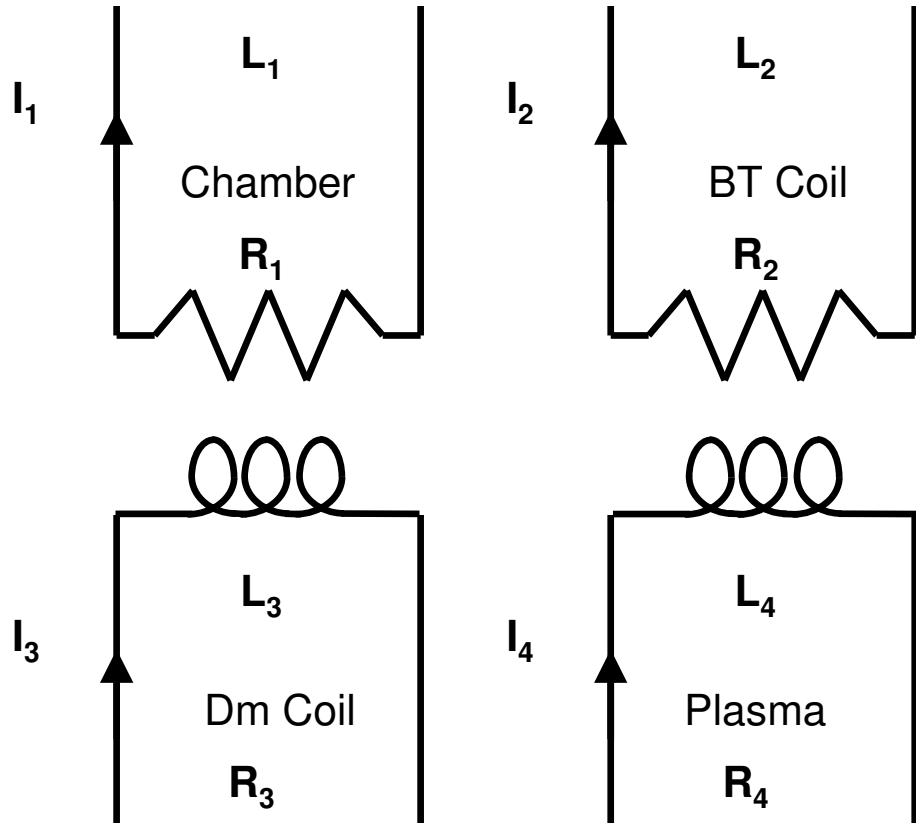


Figure 6.1: Model depicting the plasma, diamagnetic coil, BT coils, and vacuum chamber as simple circuits with resistance and inductance.

The system of the plasma, diamagnetic coil, vacuum chamber, and toroidal field coils can be modelled as a set of four linked coils with a defined resistance and inductance (Fig. 6.1), where the inductance is defined as a matrix

$$L = \begin{vmatrix} L_{11} & M_{12} & M_{13} & M_{14} \\ M_{21} & L_{22} & M_{23} & M_{24} \\ M_{31} & M_{32} & L_{33} & M_{34} \\ M_{41} & M_{42} & M_{43} & L_{44} \end{vmatrix} \quad (6.1)$$

and the subscripts refer to the coils depicted in Fig. 6.1.

The solution of this system may allow for the plasma induced image currents to be eliminated.

6.2.2 Internal Measurements

In order to further examine the residual signal in the vacuum baseline shots, it would be advantageous to mount a diamagnetic coil set inside the tokamak. Direct comparison of the internal and external measurements would provide clarification of the residual signal properties, since the internal coils would not link as strongly to the image currents in the chamber walls. Attempting to employ other measurement methods, such as the differential method would also be useful. It would be valuable to have direct comparisons between known methods of diamagnetic measurements available. At present, no such material exists. It is planned to fabricate and install diamagnetic coils for internal measurements. The internal coils will be similar to the external coils in that there will be an enclosing loop, a non-enclosing loop for toroidal field removal, and a pair of auxiliary loops for compensation of vibrations. The auxiliary loops may be installed externally due to space restrictions. The loops will be made from magnesium oxide wire (MgO) similar to that used in thermocouples and already employed in machines such as KSTAR [93]. MgO wire has excellent thermal insulation properties, and comes jacketed with stainless steel making it highly compatible with vacuum environments.

6.2.3 Improved Signal Processing

Signal processing will be achieved with a multi-stage active component design (Fig. 6.2). Particular attention is paid to gain staging and shielding to reduce the influence of noise produced by the active components themselves. Preamplification is achieved using specially designed instrumentation amplifiers. The signals are to then be mixed before being conditioned for transfer to the data acquisition system.

Instrumentation Amplifier Design

An instrumentation amplifier based on the classic 3 op amp configuration is a suitable starting point [94–97]. The 2 op amp arrangement, while available in a single IC package, was not selected due to the phase delay introduced by propagating one

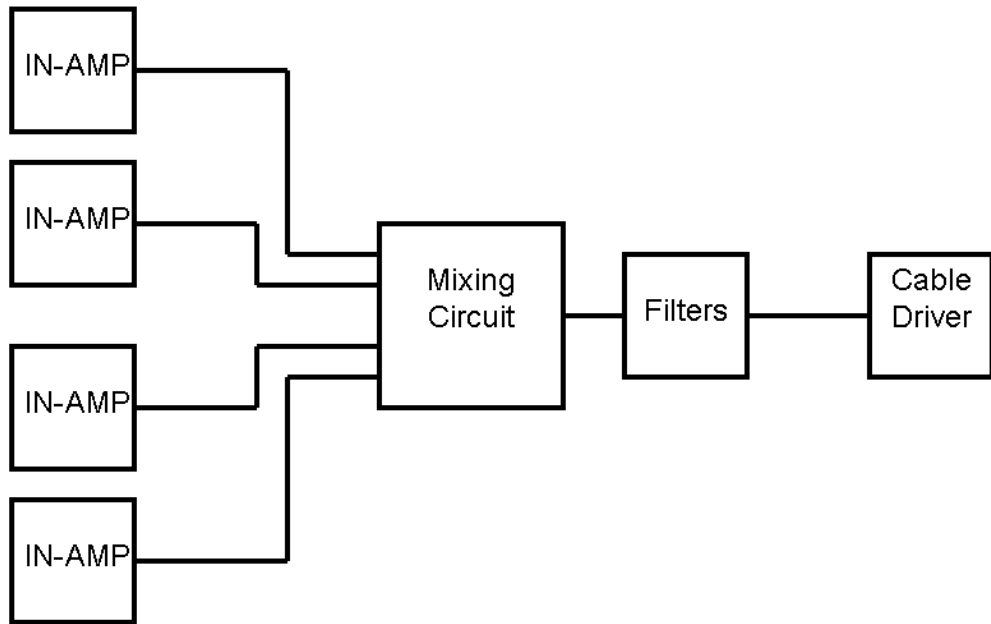


Figure 6.2: Signal Processing Block Diagram.

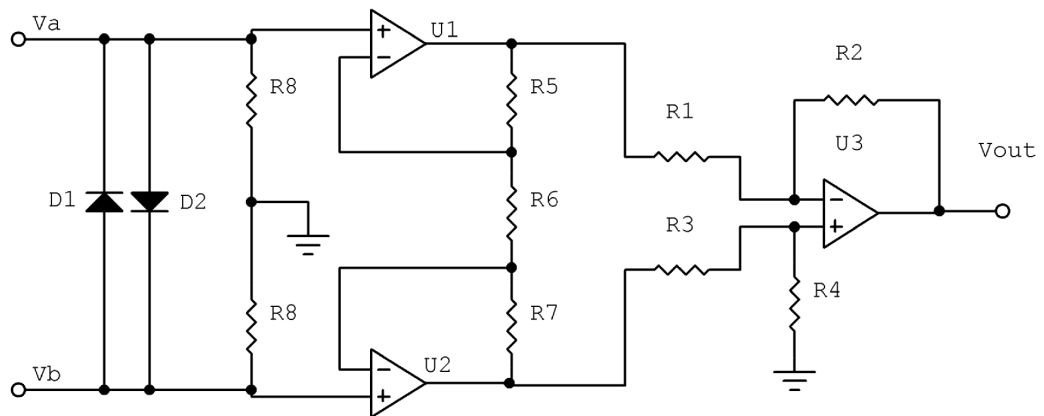


Figure 6.3: Signal Processing Block Diagram.

signal through a signal op amp prior to the subtraction that occurs at the second op amp [98]. The use of the two buffering amplifiers before the difference amplifier controls the input impedance seen by the input voltages. If the difference amplifier is used alone, the significant impedance mismatch between the inverting and non-inverting inputs of the operational amplifier can harm the common mode rejection ratio and also be a source of noise. The diodes D_1 and D_2 are used as signal limiters to provide a level of protection to the inputs of the amplifiers. The resistors designated R_8 in figure 6.3 set the impedance that the voltages from the coil (V_a and V_b) see. The output voltage, v_{out} of this amplifier is given by

$$V_{out} = -\frac{R_2}{R_1} \left(\frac{R_5 + R_6 + R_7}{R_6} \right) (v_b - v_a) \quad (6.2)$$

Requiring $R_1/R_2 = R_3/R/4$ and choosing $R_5 = R_7 = R$ reduces equation (6.2) to

$$V_{out} = -\frac{R_2}{R_1} \left(1 + \frac{2R}{R_6} \right) (v_b - v_a) \quad (6.3)$$

The AD620 instrumentation amplifier is a suitable candidate for providing the low noise signal gains required [99]. The AD620 is a single chip solution to the amplifier described above.

Signal conditioning occurs with a series of filters and a 50 Ohm driver circuit 6.4. This allows a clean, impedance matched signal to be transmitted by BNC line to the data acquisition system. The driver circuit is the final output stage of the signal processing circuitry and is based on the LM6181 Current Feedback Amplifier [100].

A suitable overall instrumentation circuit is presented in Fig 6.5, and PCB schematic in 6.6. Particular attention was paid to signal routing to minimize noise pick up. Grounding planes were routed under the IC's to further increase electrical shielding. The diodes are used to clamp input voltages and protect the instrumentation amplifiers from the large voltages recorded during the ramp up of the B_T field.

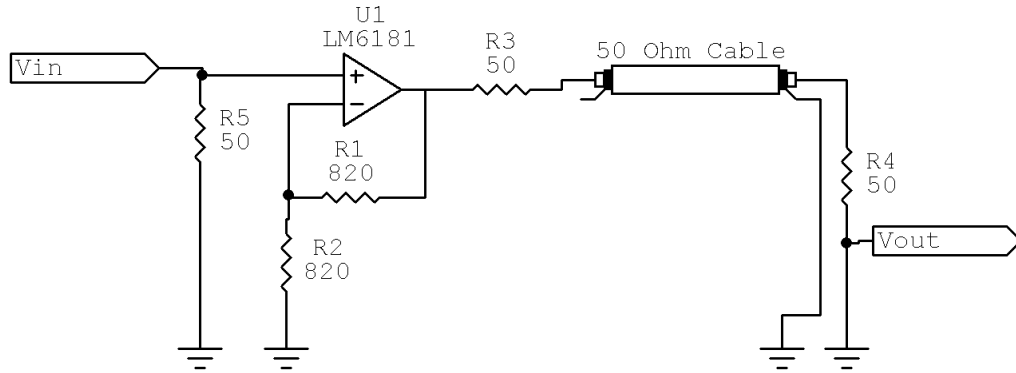


Figure 6.4: 50 Ohm Cable driver.

6.2.4 Diamagnetic Measurements in the Proposed STOR-U Tokamak

The next generation of tokamak for the Plasma Physics Laboratory is currently being proposed. STOR-U ($R = 80$ cm, $a = 36$ cm, $B_T = 1.5$ T, $I_p = 1200$ kA, $t_d = 500$ ms) will be built to allow studies with much higher plasma temperatures ($T_e = 700 - 1700$ eV, $T_i = 600 - 2500$ eV) than STOR-M. The high temperatures will be achieved by heating through neutral beam injection. STOR-U will require suitable diamagnetic measurement diagnostics to be designed and implemented as part of its diagnostics array.

The differential method using a concentric pair of MgO wires mounted internally is likely appropriate. There should be a few sets of these coils located around the torus so that the measurements can be averaged toroidally. Further, should one set become damaged or otherwise non-functional, the other sets serve as a redundant back up and measurements can continue without the need for a major opening of the chamber. Real-time measurement capability should be sought, so that STOR-U could use diamagnetic measurements of poloidal beta in the calculation of feedback parameters. The STOR-U diagnostics will require precision integration electronics, similar to those designed for KSTAR [101].

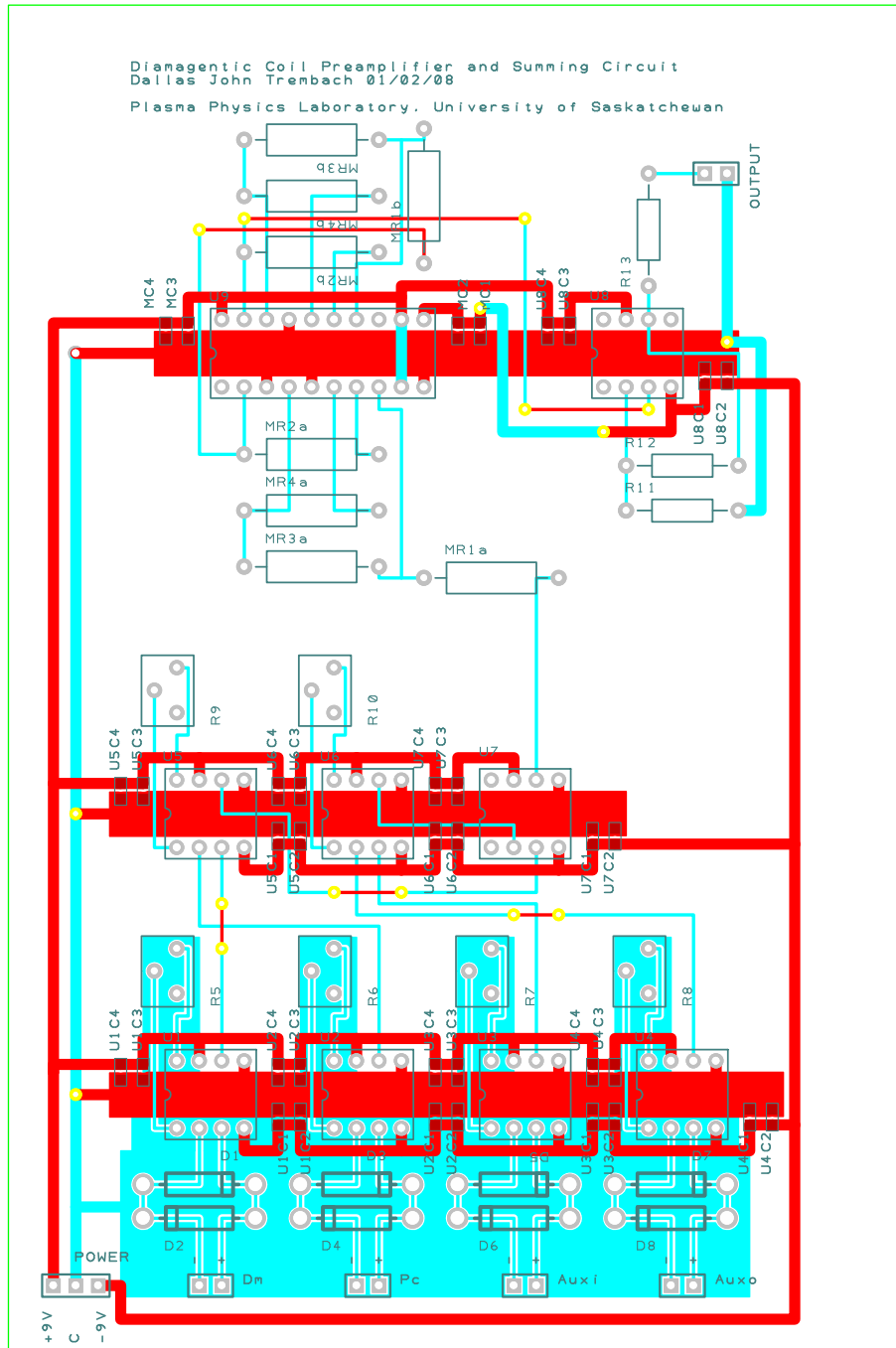


Figure 6.6: PCB track layout for improved diamagnetic measurements.

REFERENCES

- [1] I. Cook, R.L. Miller, and D.J. Ward. Prospects for economic fusion electricity. *Fusion Engineering and Design*, 63-64:25, 2002.
- [2] M. Zucchetti. The zero-waste option for nuclear fusion reactors: Advanced fuel cycles and clearance of radioactive materials. *Annals of Nuclear Energy*, 32:1584, 2005.
- [3] R. F. Post. Controlled fusion research - an application of the physics of high temperature plasmas. *Reviews of Modern Physics*, 28:338, 1956.
- [4] M. Keilhacker, A. Gibson, C. Gormezano, and P.H. Rebut. The scientific success of jet. *Nuclear Fusion*, 41:1925, 2001.
- [5] JT-60 Team. *Review of JT-60U Experimental Results in 1998*. JAERI 99-048, 1999.
- [6] R. Aymar, V.A. Chuyanov, M. Huget, Y. Shimomura, ITER Joint Central Team, and ITER Home Teams. Overview of iter-feat -the future international burning plasma experiment. *Nuclear Fusion*, 41:1301, 2001.
- [7] Y. Shimomura, R. Aymar, V.A. Chuyanov, M. Huget, H. Matsumoto, T. Mizoguchi, Y. Murakami, A.R. Polevoi, M. Shimada, ITER Joint Central Team, and ITER Home Teams. Iter-feat operation. *Nuclear Fusion*, page 309, 2001.
- [8] R. J. Thome and P.J. Heitzenroeder. Engineering features of the fusion ignition research experiment (fire). *Fusion Engineering and Design*, 58:797, 2001.
- [9] M. Trautmann, K.W. Rothe, J.Wanner, and H. Walther. Determination of the deuterium abundance in water using a cw chemical df laser. *Appl. Phys.*, 24:49, 1981.
- [10] S. Kaufman and W. F. Libby. The natural distribution of tritium. *Phys. Rev.*, 93:1337, 1954.
- [11] K. Niu. *Nuclear Fusion*. Cambridge University Press, 1989.
- [12] M. Emaami-Khonsaari. *Modelling and Control of the Plasma Position in the STOR-M Tokamak*. PhD thesis, University of Saskatchewan, 1990.
- [13] F. F. Chen. *Introduction to Plasma Physics and Controlled Fusion*. Plenum Press, New York and London, 2nd edition, 1984.

- [14] W. M. Stacey. *Fusion: An Introduction to the Physics and Technology of Magnetic Confinement Fusion*. Wiley-Interscience, 1984.
- [15] P.M. Bellan. *Spheromaks*. London: Imperial College Press, 2000.
- [16] L.A. Artsimovich. Tokamak devices. *Nuclear Fusion*, 12:215, 1972.
- [17] B.B. Kadomstev. *Tokamak Plasma: A Complex Physical System*. London: Institute of Physics Publishing, 1992.
- [18] B.B. Kadomstev, F.S. Troyon, M.L. Watkins, P.H. Rutherford, M. Yoshikawa, and V.S. Mukhovatov. Tokamaks. *Nuclear Fusion*, 30:1675, 1990.
- [19] J.A. Wesson. *Tokamaks*. Clarendon Press, Oxford, 1987.
- [20] H.P. Furth. Tokamak research. *Nuclear Fusion*, 15:487, 1975.
- [21] K.C. Mark. Diamagnetic measurements on the stor-1m tokamak. Master's thesis, University of Saskatchewan, 1993.
- [22] A. Hirose. Chapter 1 general properties of high temperature plasmas. Lecture Notes, 2007.
- [23] C. Varandas and C. Silva, editors. *Recent Results from the STOR-M Tokamak*, 17th IAEA Technical Meeting on Research Using Small Fusion Devices, Lisbon, Portugal, 22-24 October 2007, 2008. AIP Conference Proceedings Series, American Institute of Physics, Melville, NY.
- [24] O. Mitarai, A. Hirose, and H.M. Skarsgard. Alternating current tokamak reactor with ohmic ignition and bootstrap current. Technical Report PPL-120, Plasma Physics Laboratory, University of Saskatchewan, 1991.
- [25] W. Zhang, C. Xiao, G.D. Conway, O. Mitarai, A. Sarkissian, H.M. Skarsgard, L. Zhang, and A. Hirose. Improved confinement and edge plasma fluctuations in the stor-m tokamak. *Phys. Fluids B*, 4:3277, 1992.
- [26] W. Zhang, C. Xiao, and A. Hirose. Improved confinement and edge plasma fluctuations in the stor-m tokamak. *Phys. Fluids B*, 5:3961, 1993.
- [27] W. Zhang. *Improved Ohmic Confinement Induced By Turbulent Heating and Electrode Biasing in the STOR-M Tokamak*. PhD thesis, University of Saskatchewan, 1993.
- [28] C. Xiao and A. Hirose. Improved confinement induced by tangential injection of compact torus into the saskatchewan torus-modified (stor-m) tokamak. *Physics of Plasmas*, 11:4041, 2004.
- [29] S. J. Livingston. Experimental study of density fluctuations in the stor-m tokamak by small-angle microwave scattering. Master's thesis, University of Saskatchewan, 2005.

- [30] C. Xiao, S.J. Livingstone, A.K. Singh, D. Raju, G.S. Germaine, D. Liu, C. Boucher, and A. Hirose. Short wavelength density and low frequency mhd fluctuation measurements in the stor-m tokamak. IAEA Fusion Energy Conference 2006, Paper No. EX/P4-31, 2006.
- [31] M. Dreval, C. Xiao, D. Trembach, A. Hirose, S. Elgriw, A. Pant, D. Rohraff, and T. Niu. Simultaneous evolution of plasma rotation, radial electric field, mhd activity and plasma confinement in stor-m tokamak. *Plasma Physics and Controlled Fusion*, 50:095014, 2008.
- [32] G. M. R. St. Germaine. Plasma flow velocity measurements with a gundestrup probe in the stor-m tokamak. Master's thesis, University of Saskatchewan, 2006.
- [33] A. Hirose, C. Xiao, O. Mitarai, J. Morelli, and H.M. Skarsgard. Stor-m tokamak design and instrumentation. *Physics in Canada*, 62:111, 2006.
- [34] Atlas Alloys. *Catalog: Aluminum, Stainless Steels, Nickel Alloys*. Etobicoke, Ontario, 1979.
- [35] Leybold-Heraeus Vacuum Products Inc. *TMP/NT 1000 Turbomolecular Pump & Frequency Converter Manual*.
- [36] Leybold Vacuum Products Inc. *Trivac A Dual Stage Rotary Vane Pump Manual*.
- [37] Inc. Veeco Instruments. *Automatic Pressure Controllers APC-1000 APC-2000 Operation and Maintenance Manual*.
- [38] Inc. Veeco Instruments. *Precision Leak Valve PV-10 Operation & Maintenance*.
- [39] Inc. Powerex. *Data Sheet, TA20 1800A Phase Control SCR*, 2006.
- [40] ABB Switzerland Ltd. *Data Sheet, 5STP33L2800 Phase Control Thyristor*, 2002.
- [41] RCA Tube Division. *Data Sheet, Ignitron 5551, Size B*, 1946.
- [42] J. E. Morelli. *PLASMA POSITION CONTROL IN THE STOR-M TOKAMAK: A FUZZY LOGIC APPROACH*. PhD thesis, University of Saskatchewan, 2003.
- [43] D.Q. Hwang, R.D. Horton, S. Howard, R.W. Evans, and S.J. Brockington. Advances in ctix accelerator study. *Journal of Fusion Eenergy*, 26:81, 2007.
- [44] A. Graf, S. Howard, R. Horton, M. May, and D. Hwang. Visible spectrometer at the compact toroid injection experiment, the sustained spheromak plasma experiment and the alcator c-mod tokamak for doppler width and shift measurements. *Review of Scientific Instruments*, 77:10F125, 2006.

- [45] P.B. Parks. Refueling tokamaks by injection of compact toroids. *Physical Review Letters*, page 1364, 1988.
- [46] L.J. Perkins, S.K. Ho, and J.H. Hammer. Deep penetration fuelling of reactor-grade tokamak plasmas with accelerated compact toroids. *Nuclear Fusion*, 38:1365, 1988.
- [47] D. Liu. *Vertical Compact Torus Injection Into the STOR-M tokamak*. PhD thesis, University of Saskatchewan, 2006.
- [48] C. Xiao, T. Niu, J.E. Morelli, C. Paz-Soldan, M. Dreval, S. Elgriw, A. Pant, D. Trembach, and A. Hirose. Design and initial operation of multichord soft x-ray detection arrays on the stor-m tokamak. *Review of Scientific Instruments*, page 10E926, 2008.
- [49] M.A. Heald and C.B. Wharton. *Plasma Diagnostics with Microwaves*. New York: John Wiley & Sons, Inc, 1965.
- [50] M. Emaami, O. Mitarai, and S.W. Wolfe. Plasma physics laboratory report. Technical Report PPL-86, Univeristy of Saskatchewan, 1986.
- [51] R.D. Hazeltine, F.L. Hinton, and M.N. Rosenbluth. Plasma transport in a torus of arbitrary aspect ratio. *Physics of Fluids*, 16:1645, 1973.
- [52] L. Spitzer. *Physics of Fully Ionized Gasses*. Interscience, New York, 1956.
- [53] M.C. Zarnstroff, K. McGuire, M.G. Bell, B. Grek, D. Johnson, D. McCune, H. Park, A. Ramsey, and G. Taylor. Parallel electric resistivity in the tftt tokamak. *Phys. Fluids B*, page 1852, 1990.
- [54] I. H. Hutchinson. *Principles of Plasma Diagnostics*. Cambridge University Press, Cambride, England, second edition, 2002.
- [55] M.E. Foord, E.S. Marmor, and J.L. Terry. Multichannel light detector system for visible continuum measurements on alcator c. *Review of Scientific Instruments*, 53:1407, 1982.
- [56] H. Kuwahara. *Experimental Studies on Turbulent Heating in STOR 1*. PhD thesis, University of Saskatchewan, 1980.
- [57] I.H Hutchinson. The measurement of the poloidal beta in the It-3 tokamak. *Plasma Physics*, 18:246, 1976.
- [58] K.A. Razumova. Measurement of the plasma energy in a tokamak machine by the change in longitudinal magnetic flux. *J. Nucl. Energy Part C Plasma Phys.*, 8:791, 1966.
- [59] M. Maeno, S. Sengoku, S. Yamamoto, N. Suzuki, T. Yamuchi, H Kawashima, and Y. Miura. Diamagnetic measurement of jft-2 plasma heated by neutral beam injection. *Jpn. J. Appl. Phys*, 23:1236, 1984.

- [60] B. Shen, Y. W. Sun, N. Wan, and J. P. Qian. Poloidal beta and internal inductance measurement on ht-7 superconducting tokamak. *Review of Scientific Instruments*, 78:093501, 2007.
- [61] S.K. Saha, R. Kumar, and A. K. Hui. Measurement of plasma diamagnetism in the sinp tokamak by a flux loop system inside the vacuum vessel. *Review of Scientific Instruments*, 72:4289, 2001.
- [62] X.B. Li and R.C. Cross. Measurement of plasma diamagnetism by a coil located inside a conducting wall. *Review of Scientific Instruments*, 65:2623, 1994.
- [63] A.N. Aleynikov, V.S Cherkassky, B.A. Knyazev, and B.N. Breizman. On the interpretation of diamagnetic loop measurements for a current-carrying plasma column in a conducting chamber. *Physics of Plasmas*, 1:1117, 1993.
- [64] J.H. Booske, W.D. Getty, and R.M. Gilenbach. Extended frequency compensation of a diamagnetic loop. *Plasma Physics and Controlled Fusion*, page 991, 1986.
- [65] E.J. Strait. Magnetic diagnostic system of the diii-d tokamak. *Review of Scientific Instruments*, page 023502, 2006.
- [66] G. Tonetti, J. P. Christiansen, and L. de Kock. Measurement of the energy content of the jet tokamak plasma with a diamagnetic loop. *Review of Scientific Instruments*, 57:2087, 1986.
- [67] A. Manini, J-M. Moret, S. Alberti, T.P. Goodman, and M.A. Henderson. Modulated ech power absorption measurements using a diamagnetic loop in the tcv tokamak. *Plasma Physics and Controlled Fusion*, page 139, 2002.
- [68] G. Chitarin, F. Basso, V. Coccolese, S. Peruzzo, N. Pomaro, T. Edlington, C. Sowden, S. Cramp, K. Fullard, and JET-EFDA contributors. Design of ex-vessel magnetic probes for jet-ep. *Fusion Engineering and Design*, 74:727, 2005.
- [69] T Yamaguchi et al. The effect of net toroidal current on the measurement of diamagnetic beta value in heliotron plasma. *Plasma Physics and Controlled Fusion*, 48:L73, 2006.
- [70] J.-M. Moret, F. Buhlmann, and G. Tonetti. Fast single loop diamagnetic measurements on the tcv tokamak. *REVIEW OF SCIENTIFIC INSTRUMENTS*, 74:4634, 2003.
- [71] V. Coccolese, R. Albanese, H. Altmann, F. Basso, A. Cenedese, and G. Chitarin et al. Design of new magnetic sensors for jet. *Review of Scientific Instruments*, 75:4311, 2004.
- [72] L. Zeng, B. Wan, and J. Qian. Diagnostics of internal inductance in ht-7. *Plasma Science and Technology*, page 991, 2001.

- [73] Seong-Heon Seo and J. G. Bak. Diamagnetic flux measurement without a compensation coil in the hanbit mirror. *REVIEW OF SCIENTIFIC INSTRUMENTS*, 76:043501, 2005.
- [74] E. Joffrin and P. Defrasne. Differential method for the real time measurement of the diamagnetic β and interal inductance in tore supra. *Review of Scientific Instruments*, 73:2266, 2002.
- [75] T. Wijands, D. Van Houtte, G. Martin, X. Litaudon, and P. Froissard. Feedback control of the current profile on tore supra. *Nuclear Fusion*, 37:777, 1997.
- [76] O. Barana, A. Murari, E. Joffrin, F. Sartori, and Contributors to the EFDA-JET Workprogramme. Real-time calculation of plasma parameters for feedback control in jet. *Nuclear Fusion*, 44:335, 2004.
- [77] S. W. Wolfe. *The STOR-1M Tokamak: Experiments on Current Reversal and Fast Current Ramping*. PhD thesis, University of Saskatchewan, 1988.
- [78] A. H. Sarkissian. *Turbulent Heating Studies on the STOR-1M Tokamak*. PhD thesis, University of Saskatchewan, 1989.
- [79] M. Haegi and F. Sand. Compensated coil system for measuring the plasma diamagnetism in toroidal devices. *Plasma Physics*, 17:997, 1975.
- [80] J.D. Jackson. *Classical Electrodynamics*. New York: Wiley, 1975.
- [81] Ramo, Whinnery, and Van Duzer. *Fields and Waves in Communications Electronics*. New York: John Wiley & Sons, Inc, 1994.
- [82] D. Griffiths. *9. Electromagnetic Waves in Alison Reeves (ed): Introduction to Electrodynamics, 3rd edition*. New Jersey: Prentice Hall, 1999.
- [83] F. Bottiglioni. Influence of metallic walls on plasma diamagnetic measurements. *Plasma Physics*, 12:131, 1969.
- [84] M.A.Rothman. Research notes: Measurement of plasma diamagnetism by a coil located near a conducting wall. *Plasma Physics*, 10:86, 1968.
- [85] A.D. Whalen. *Detection of Signals in Noise*. New York: Academic Press, 1971.
- [86] R. Morrison. *Grounding and Shielding Techniques in Instrumentation*. New York: John Wiley & Sons, Inc, 1977.
- [87] R.F. Ficchi. *Electrical Interference*. New York: Hayden Book Company, Inc., 1964.
- [88] Conduit Electrical M'F'G. Co. *Useul Information for the Application of Electrical Protective Devices, 3rd Edition*, 1921.

- [89] D. A. Bell. *Statistical Methods in Electrical Engineering*. London: Chapman and Hall Ltd., 1953.
- [90] National Instruments. *Data Sheet, NI 6123, NI 6122, NI 6133, NI 6132*, 2005.
- [91] LeCroy. *Operating Instructions, LeCroy Model 8212 Data Logger*, 1983.
- [92] R. Raman, F. Martin, E. Haddad, M. St-Onge, C. Côté G. Abel, N. Richard, N. Blanchard, H.H. Mai, B. Quirion, J.-L LaChambre, J.-L. Gauvreau, G. W. Pacher, R. Décoste, P J. Gierszewski, D. Q. Hwang, A. Hirose, S. Savoie, B.-J. LeBlanc, H. McLean, C. Xiao, B. K. Stansfield, A. Côté, D. Michaud, and M. Chartre. Experimental demonstration of tokamak fueling by compact toroid injection. *Nuclear Fusion*, 37:967, 1997.
- [93] S.G. Lee and J.G. Bak. Magnetic diagnostics for korea superconducting tokamak advanced research. *Review of Scientific Instruments*, page 439, 2001.
- [94] R. E. Simpson. *Introductory Electronics for Scientists and Engineers*. Allyn and Bacon, Inc., second edition, 1987.
- [95] R. C. Dorf and R. H. Bishop. *Modern Control Systems*. Addison-Wesley Longman Publishing Co., Inc., 7th edition, 1994.
- [96] B. P. Lathi. *Signal Processing and Linear Systems*. Berkeley-Cambridge Press, 1998.
- [97] R.J. Smith and R.C. Dorf. *Circuits, Devices And Systems*. John Wiley & Sons, Inc., 5th edition, 1992.
- [98] C. Kitchin and L. Counts. *A Designer's Guide to Instrumentation Amplifiers*. Analog Devices, second edition, 2004.
- [99] Analog Devices. *Data Sheet, AD620 Low Cost, Low Power Instrumentation Amplifier*, 1999.
- [100] National Semiconductor. *Data Sheet, LM6181 100mA, 100MHz Current Feedback Amplifier*, 2004.
- [101] J. G. Bak, S.G. Lee, E.M. Ga, and D. Son. Characteristics of the integration system for the kstar magnetic diagnostics. *33rd EPS Conference on Plasma Phys. Rome, 19 - 23 June 2006 ECA*, 39I:P-2.179I, 2006.

APPENDIX A

INSTALLATION NOTES FOR THE DIAMAGNETIC COIL

A.1 Diamagnetic Coil

A.1.1 Parameters

The diamagnetic coil installed is based on the design presented in Haegi (Fig. A.1) [79] and subsequently implemented on the STOR-1M [21]. The coil form is constructed from 1.2 cm thick phenolic, and is a split ring of inner diameter 34.7 cm and outer diameter 37.8 cm. 1 mm deep grooves were cut into the form to allow placement of 28 AWG magnet wire windings. There are two single turn flux loops of diameters 34.95 cm and 37.55 cm, enclosing areas of approximately 959 cm² and 1776 cm², respectively. An 8 turn compensation coil is wound through both halves of the form, with inner and outer radii of $r_i = 47.55$ cm and $r_o = 17.475$ cm. The effective area enclosed by the primary compensation windings is approximately 5960 cm². Each half of the form contains an 8 turn auxiliary compensation coil (see figure A.1).

A.1.2 Coil Winding Notes

To wind the coils, place the form on a work bench and tape down with several strips of electrical tape (see figure A.2). Install the coil windings into the grooves, successively lifting and replacing the tape strips as required (see figure A.3). This ensures the coil remains in the groove during winding. Use Cyanoacrylate based adhesive to seal the coils into the form.

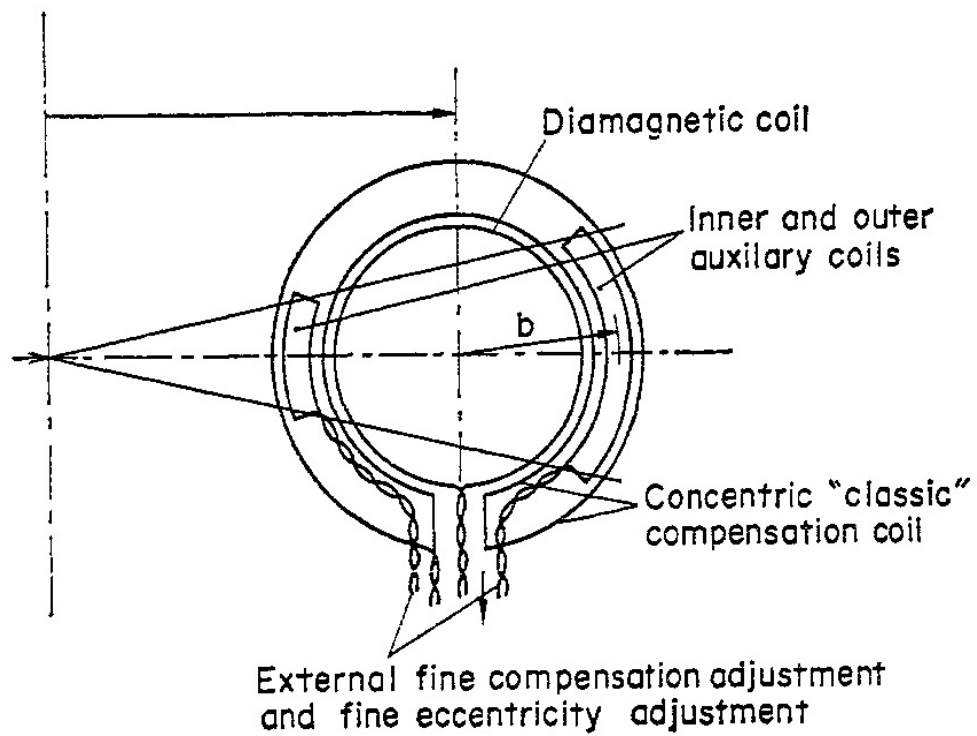


Figure A.1: Auxiliary (vibrational) compensation coils and primary compensation coils.

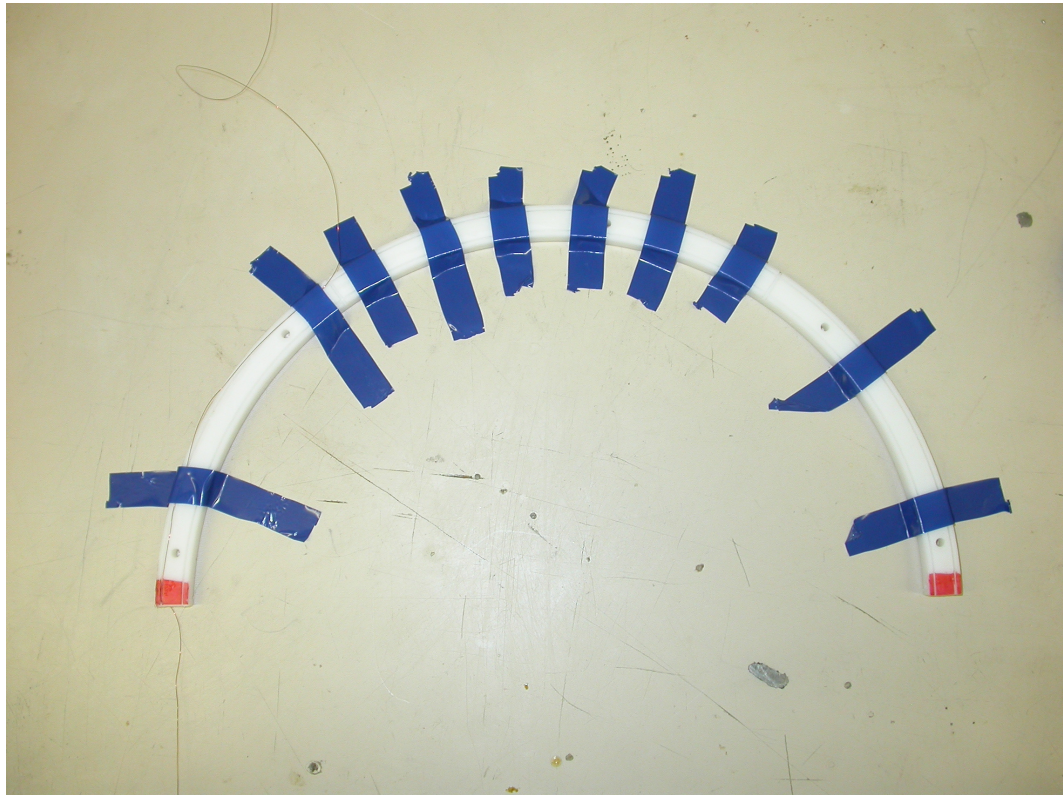


Figure A.2: Coil form with tape strips for coil winding. In this figure, an auxiliary compensation coil is being wound.



Figure A.3: Coil winding turning corners in the form grooves. A piece of tape is lifted to illustrate the winding method.

A.1.3 Installation Figures



Figure A.4: Diamagnetic coil installed on STOR-M

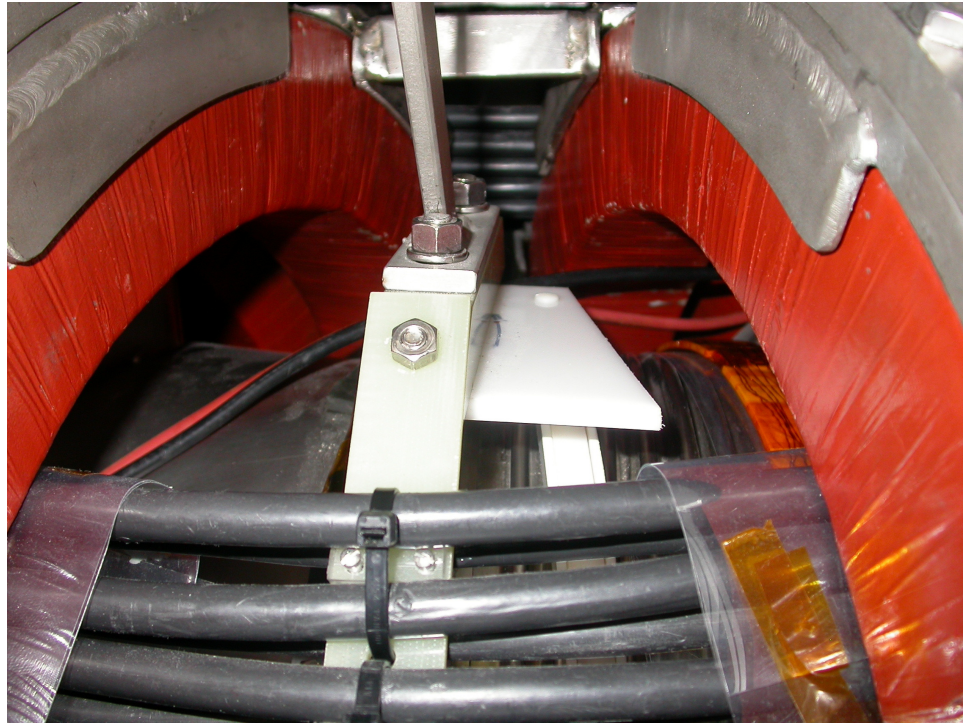


Figure A.5: Upper mounting point for Diamagnetic Coil. The mounts are connected to the yokes of the machine, isolating the coil form from the chamber. Lower mount is identical.

A.1.4 Installation Notes

1. The coil can be pivoted around the joint at the top of the form where the coil loops pass through, but must be done so carefully.
2. Beginning from the top of the chamber, insert the bottom of the inside form and slide in down along the bellows, keeping the outside form at a right angle to the inside form.
3. With the inside form in place, the outside form can be turned into place.
4. Secure the coil to the mounts (see Figure A.5).
5. Route the leads exiting from the bottom of the forms below the bellows and the TF interconnects.
6. Twist the diamagnetic coil leads together, closing the loop and forming a twisted pair lead.
7. Install the side shields using nylon nuts and bolts. The side shields are used to hold the two forms together, as well as to protect the cables.
8. Shrink wrap the coil leads.
9. Install a conducting braid over the shrink wrap
10. Shrink wrap the conducting braid
11. Ground the conducting braid
12. Install DA-15 connector

A.1.5 Removal Notes

CAUTION: Before removing the coil from the tokamak the wiring harness must be disassembled and untwisted. Failure to do so will cause damage to the coils during removal.

1. Remove DA-15 connector from signal box.
2. Disconnect leads from DA-15 (be careful to label the wires).
3. Remove heat shrink from cable.
4. Remove conducting braid from cable.
5. Remove inner heat shrink, revealing diamagnetic coil leads.
6. Untwist the inner and outer coil leads.
7. Remove side shields from coil form (nylon nuts and bolts).



Figure A.6: BNC Breakout box

8. Remove nylon screws from top and bottom mounts (one each, see figure A.5).
9. The coil separates into two pieces, joined at the top by the coil windings. The coil can be pivoted around this joint, but must be done so carefully.

A.2 Signal Processing

A.2.1 BNC Breakout Box

The BNC Breakout Box is a testing tool for adapting the DA 15 output of the coil assembly to BNC connectors. The box consists of 5 isolated BNC connectors inside a shielded enclosure, A male DA 15 connector, and a grounding post.

A.2.2 DA 15 Pinout Diagram

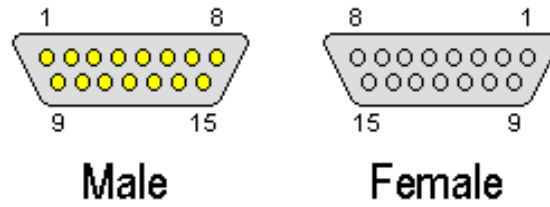


Figure A.7: DA 15 pin numbering for male and female connectors

| Pin | Description |
|-----|-----------------------------------|
| 1 | Inner Diamagnetic Coil |
| 2 | Outer Diamagnetic Coil |
| 3 | Primary Compensation Coil |
| 4 | Outer Auxiliary Compensation Coil |
| 5 | Inner Auxiliary Compensation Coil |
| 6 | No Connection |
| 7 | No Connection |
| 8 | No Connection |
| 9 | Inner Diamagnetic Coil |
| 10 | Outer Diamagnetic Coil |
| 11 | Primary Compensation Coil |
| 12 | Inner Auxiliary Compensation Coil |
| 13 | Outer Auxiliary Compensation Coil |
| 14 | No Connection |
| 15 | No Connection |

Table A.1: DA 15 Pinout (26 July 2007)